remote sensing

MDPI

Article

Towards the Mitigation of Discrepancies in Sea Surface Parameters Estimated from Low- and High-Resolution Satellite Altimetry

Christopher K. Buchhaupt [1,*], Alejandro Egido [2], Douglas Vandemark [3], Walter H. F. Smith [4], Luciana Fenoglio [5] and Eric Leuliette [4]

1 Earth System Science Interdisciplinary Center, Cooperative Institute for Satellite Earth System Studies, University of Maryland, College Park, MD 20740, USA
2 European Space Research and Technology Centre, European Space Agency, 2201 AZ Noordwijk, The Netherlands; alejandro.egido@esa.int
3 Institute for the Study of Earth, Oceans and Space, University of New Hampshire, Durham, NH 03824, USA; doug.vandemark@unh.edu
4 Center for Satellite Applications and Research, National Oceanographic and Atmospheric Administration, College Park, MD 20740, USA; walter.hf.smith@noaa.gov (W.H.F.S.); eric.leuliette@noaa.gov (E.L.)
5 Astronomical, Physical and Mathematical Geodesy, University of Bonn, 53115 Bonn, Germany; fenoglio@geod.uni-bonn.de
* Correspondence: cbuchhau@umd.edu

Abstract: In this study, we present an extension to existing numerical retrackers of synthetic-aperture radar (SAR) altimetry signals. To our knowledge at the time of writing this manuscript, it offers the most consistent retrieval of geophysical parameters compared to low-resolution mode (LRM) retracking results. We achieve this by additionally estimating the standard deviation of vertical wave-particle velocities σ_v and a new parameter u_x, linked to a residual Doppler in the returned radar echoes, which can be related to wind speed and direction. Including this new parameter into the SAR stack retracker mitigates sea surface height estimation errors by up to two centimeters for Sentinel-6MF SAR mode results. Additionally, we found a closed-form equation to describe u_x as a function of eastward and northward wind variables, which allows mitigating the effects of this parameter on a SAR stack within level 1B processing and generating a lookup table to correct sea surface height estimates in SAR mode. This additionally opens up the door to estimating the wind speed and direction from SAR altimetry stacks. Additionally, we discuss how this new retracker performs with respect to different planned future baseline processor changes of Sentinel-6MF, namely F09 and F10, by attempting to imitate their level 2 processing. This is achieved by processing cycles 017 to 051 (nearly a full year) of Sentinel-6MF level 1A data on a global scale. We observe that the new retracking method is, on average, more accurate with respect to LRM. However, there is a slight increase in measurement noise due to the introduction of an additional parameter. To ensure that the results of the new retracker are not biased, we retrack using both the new method and the SINCS-OV ZSK retracker on Sentinel-6MF stack data produced in a Monte Carlo simulation. We analyze the simulation results with respect to accuracy, precision, and correlations between estimated parameters. We show that the accuracy of the new retracker is better than SINCS-OV ZSK but less precise, which could be related to higher correlation coefficients—especially with respect to the new parameter u_x—between estimated parameters.

Keywords: delay-Doppler altimetry; wave-particle motions; retracking; sea surface height; significant wave height; wind speed; wind direction

Citation: Buchhaupt, C.K.; Egido, A.; Vandemark, D.; Smith, W.H.F.; Fenoglio, L.; Leuliette, E. Towards the Mitigation of Discrepancies in Sea Surface Parameters Estimated from Low- and High-Resolution Satellite Altimetry. *Remote Sens.* **2023**, *15*, 4206. https://doi.org/10.3390/rs15174206

Academic Editor: Dusan Gleich

Received: 29 June 2023
Revised: 16 August 2023
Accepted: 18 August 2023
Published: 27 August 2023

1. Introduction

For several decades, nadir-looking satellite radar altimeter missions have been routinely used to monitor ocean surface heights and sea state parameters. In a process called

"retracking", parameterized models for the expected radar power returned from a randomly rough surface are fit to the averages of radar pulse echoes in order to retrieve the parameters known as sea surface height (SSH) and significant wave height (SWH), and the normalized radar cross-section, σ_0, from which wind speed is derived. The parameters are sensitive to an area of ocean surface called the measurement "footprint".

In the first few decades of altimetry, only incoherent averaging of pulse echoes was used, a technique now called low-resolution mode (LRM). The parametric model for LRM is known as the Brown model [1], and the retracker for LRM is the MLE3/4 retracker [2], where MLE stands for the maximum likelihood estimator, and the number afterward denotes the number of estimated parameters. The LRM footprint is in a circle of a few km in diameter, and the diameter increases as SWH increases [3].

In the last 12 years, SAR altimeter missions have furnished radar echoes that can be coherently processed to narrow the footprint in the direction of spacecraft flights. fully focused SAR (FF-SAR) altimetry [4] takes aperture synthesis to the maximum limit and can measure water surface heights in rivers and canals that are very narrow (a few meters) in the direction of flight [5]. However, over the open ocean, the standard practice, known as unfocused SAR (UF-SAR) or Delay/Doppler altimetry [6], synthesizes an aperture for only a few milliseconds of the flight, narrowing the footprint to about 300 m in the flight direction while leaving the across-flight dimension the same size as for LRM altimetry. This standard approach to ocean SAR altimetry is the concern of this paper; here, to distinguish it from LRM altimetry, it is simply called "SAR" altimetry. The SAMOSA2 retracker [7]—named after the project "SAR Altimetry Mode Studies and Applications over Ocean, Coastal Zones and Inland Water (SAMOSA)"—retrieves SSH, SWH, and wind speed from SAR altimeter radar echo power displayed as a one-dimensional function of the two-way travel time of the radar pulse.

Geophysical parameters retrieved from SAR altimetry can be more precise than those retrieved from LRM altimetry, but LRM and SAR retrievals may have different accuracies and biases. SAR altimetry exploits Doppler shifts arising from relative motion between the altimeter antenna and the radar scattering points on the sea surface; this may make the SAR parameter estimates sensitive to the direction of ocean surface motions caused by winds and waves. LRM gives equal weight to radar scatterers lying at all azimuths within the circular measurement area; thus, LRM parameter estimates should be independent of any angle between wind or wave propagation and the spacecraft flight direction.

The first generation of SAR altimeters, CryoSat-2 and Sentinel-3, could operate in either LRM or SAR modes, but only by one mode at a time, exclusive of the other mode. Differences in LRM and SAR estimates, if any, had to be found by comparing SAR mode estimates to observations from so-called pseudo-LRM signals, which mimic LRM, but are computed in SAR mode. In this way, it was found that the CryoSat-2 SAR mode SWH retrievals differed from pseudo-LRM by up to 20 cm. Buchhaupt [8] showed that the standard deviation of vertical wave-particle velocities σ_v would blur the Doppler spectrum exploited in the SAR mode; this would lead to biased SWH estimates because one-dimensional SAR retrackers that are in use would not be able to distinguish between the effect of SWH and the effect of σ_v.

To improve the accuracy of SWH retrievals from SAR altimetry, Buchhaupt [8] introduced the SINCS-OV (signal model involving numerical convolutions for SAR introducing orbital velocities) retracker, which estimates the geophysical parameters and σ_v by fitting a model to a two-dimensional "stack" displaying radar echo power as a function of both two-way travel time and Doppler frequency. While this approach mitigated the differences between pseudo-LRM and SAR estimates of SWH, the σ_v estimates did not agree well with observations from buoys and model forecasts from the European Centre for Medium-Range Weather Forecasts (ECMWF). This issue was addressed in Buchhaupt et al. [9] by considering that the SAR altimeter may be sensitive to vertical wave motion only where wave slopes are close to radar incidence angles, making the observable σ_v smaller than the actual σ_v by a factor a_v, which depends mainly on wave steepness, S_m; correcting σ_v estimates

from SINCS-OV for the a_v effect resulted in σ_v values consistent with ECMWF and buoy measurements in the German Bight.

Although the σ_v effect with its a_v correction seemed to solve the problem of the SWH estimation, Raynal et al. [10] found SSH anomaly differences between Sentinel-3 SAR retrievals and pseudo-LRM retrievals. The geographical distribution of these differences suggested a correlation with the global pattern of the north–south wind speed.

With the launch of Sentinel-6MF, it has been possible to simultaneously make geophysical retrievals from both LRM and SAR modes, enabling a direct and global investigation of discrepancies in the two types of retrievals. We found that the differences in SSH retrieved from Sentinel-6MF by LRM and by SAR are linked to both the wind speed and the wind direction relative to the flight direction [11]; see Figures 1 and 2. This effect arises through a wave Doppler-induced bias, as the wind speed determines the wave slopes and the orbital velocity of water particles [12].

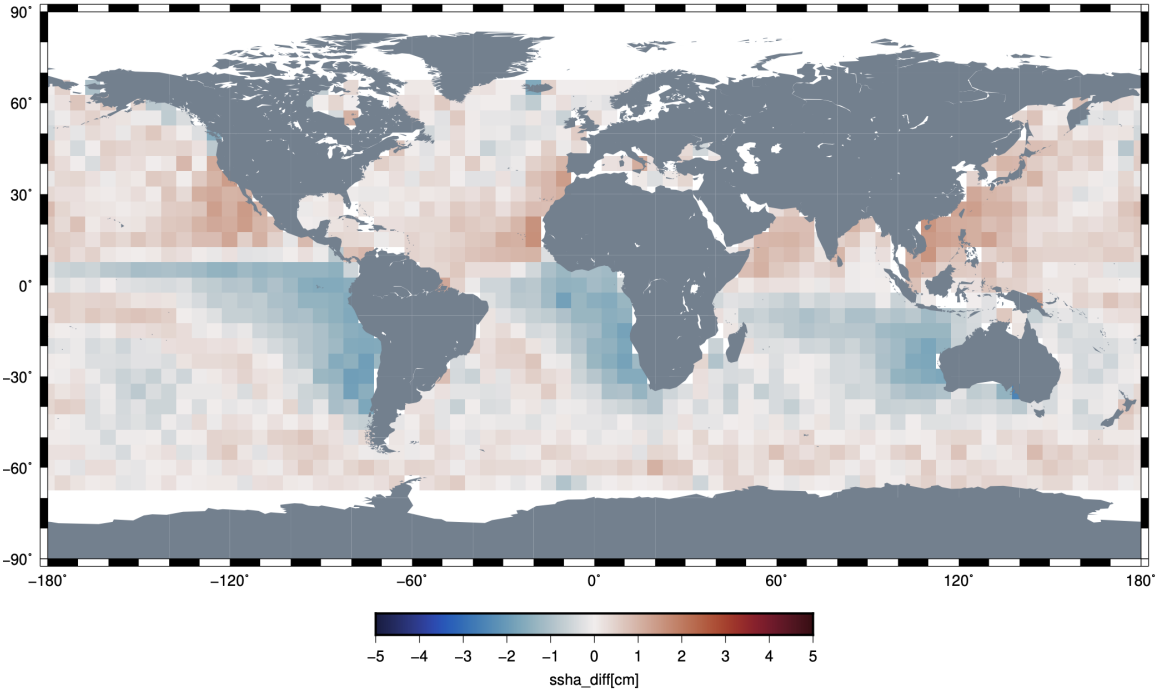

Figure 1. Sentinel-6MF sea surface height anomaly differences between SAR and LRM data as presented by [11]. Descending passes are denoted by a negative sign.

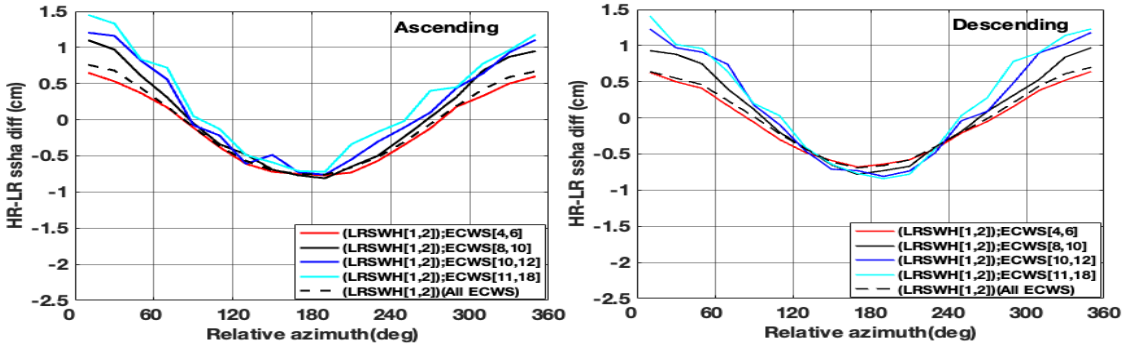

Figure 2. Bias between Sentinel-6MF SAR and LRM in SSH for LRM SWH (LRSWH) values between one and two meters and different ECMWF wind speeds (ECWS) linked to the relative wind directions, with respect to the satellite heading [11]. (**Left**): Ascending passes. (**Right**): Descending passes.

This study focuses on mitigating these SSH inconsistencies. As Sentinel-6MF is the new reference mission after Jason-3, this study will discuss the results of this mission to provide an initial perspective. In future studies, other SAR altimetry missions will be considered as well.

Section 2 discusses how these velocities are introduced into the SAR stack model and Section 3 shows how this new parameter is implemented in the SAR altimetry stack model. Section 4 shows that atmospheric refraction has the same effect on a stack as horizontal velocities and provides a formulation to introduce this effect in SAR data processing. In Section 5, we discuss the implementation choices of the Sentinel-6MF processing campaign presented in this study. The same processing parameters are then used in the Monte Carlo processing presented in Section 6. These simulations are performed to ensure that the proposed retracking scheme provides bias-free estimates. Additionally, the Monte Carlo runs provide important information about the reachable accuracy, precision, and correlation between estimated parameters. In Section 7, we discuss the results of the Sentinel-6MF processing campaign, and afterward we present our conclusions.

2. Including Horizontal Velocities in an Analytical Description of SAR Altimetry Signals over a Random Sea Surface

In SAR altimetry, it is necessary to describe the echoes scattered off the ocean surface as a two-dimensional delay–Doppler map (DDM) (or stack) in both the time delay, with respect to the tracking range gate (τ), and Doppler frequency (f_D) domains. In Buchhaupt et al. [13], Buchhaupt [8], and Buchhaupt et al. [14], we first introduced the representation of the DDM as a fast convolution method, which we aim to expand in this study. In the fast convolution approach, we define the backward Fourier transform (FT) from f_D to the slow time, t_s, and the forward FT from τ to the frequency f of the SAR altimetry stack [14]. After these FTs, the DDM can be described as the multiplication of three terms [14]:

$$\hat{\hat{P}}\left(f, t_s + \tfrac{f}{s}\right) = F\hat{\hat{S}}SR(f, t_s)P\hat{\hat{T}}R\left(f, t_s + \tfrac{f}{s}\right)P\hat{\hat{D}}F(f, t_s) \tag{1}$$

where s is the chirp or sweep signal slope and $F\hat{\hat{S}}SR(f, t_s)$ is the flat sea surface response (FSSR), describing the altimeter impulse response in the slow-time/frequency domain. $P\hat{\hat{T}}R(f, t_s)$, the point target response (PTR), describes the radar response to a single isotropic scatterer. $P\hat{\hat{D}}F(f, t_s)$ introduces a rough random sea surface, which mainly causes range-smearing due to random elevations and azimuth-smearing due to random vertical wave-particle velocities. For the sake of convenience, we provide the computations of all three terms in Appendices A–C.

The benefit of Equation (1) compared to SAR altimetry signal representations in the τ/f_D domain is that the FSSR and PTR terms are constant for each DDM. Only the probability density function (PDF) term contains geophysical parameters and, therefore, needs to be evaluated in every iteration of a nonlinear optimization process. Additionally, no convolutions need to be solved and no approximation of the PTR is necessary.

To introduce vertical and horizontal velocities on the sea surface, we define—similar to [15]—a Doppler pulsation term, Ω_L, containing horizontal and vertical dynamics of a larger scattering surface element located at the along-track coordinate x and across-track coordinate y, which, according to [12], dominate the Doppler shifts at small incidence angles, such as for nadir-looking altimeters:

$$\Omega_L = \frac{2}{\lambda_c}\left(z_t - \alpha_x c_x \frac{x}{h_s} - \alpha_y c_y \frac{y}{h_s}\right) \tag{2}$$

where z_t denotes the vertical wave-particle velocities, λ_c denotes the carrier wavelength of the emitted signal, h_s denotes the satellite altitude with respect to the reference surface, α_x denotes the along-track curvature coefficient, α_y denotes the across-track curvature

coefficient, c_x denotes the along-track horizontal sea surface velocities, and c_y denotes the across-track horizontal sea surface velocities.

The line of sight variance of Ω_L, together with the nonlinear sea surface elevation η and slopes η_x/η_y—under the assumption that horizontal wave-particle velocity components are negligible for nadir-looking altimeters—were thoroughly discussed in [9]. Therefore, this study focuses on the mean line of sight Doppler pulsation, which can be written with $\frac{x^2}{h_s^2} \ll 1$ and $\frac{y^2}{h_s^2} \ll 1$ as follows:

$$\bar{\Omega}_L = E\left[\Omega_L \middle| \left(z_x = \frac{\alpha_x x}{h_s}, z_y = \frac{\alpha_y y}{h_s}\right)\right] \tag{3a}$$

$$\approx \frac{2}{\lambda_c} \underbrace{\left(a_{vx}\frac{\sigma_v}{\sigma_x} - c_y\right)}_{u_x} \frac{\alpha_x x}{h_s} \tag{3b}$$

$$+ \frac{2}{\lambda_c} \underbrace{\left(a_{vy}\frac{\sigma_v}{\sigma_y} - c_x\right)}_{u_y} \frac{\alpha_y y}{h_s} \tag{3c}$$

where a_{vx} and a_{vy} are auxiliary parameters mostly depending on the correlation vertical wave-particle velocities and along-track or across-track wave slopes. They are given as [9]:

$$a_{vx} = \frac{\rho_{xt} - \rho_{yt}\,\rho_{xy}}{1 - \rho_{xy}^2} \tag{4a}$$

$$a_{vy} = \frac{\rho_{yt} - \rho_{xt}\,\rho_{xy}}{1 - \rho_{xy}^2} \tag{4b}$$

where ρ_{xt} is the correlation coefficient between along-track wave slopes and vertical wave-particle velocities, ρ_{yt} is the correlation coefficient between across-track wave slopes and vertical wave-particle velocities, ρ_{xy} is the correlation coefficient between along-slopes and across-track wave slopes.

In Equation (3), u_x and u_y behave as horizontal sea surface velocities in along- and across-track directions. Even so, they also contain vertical components of wave velocities at a given wave slope. Therefore, u_x can be referred to as he mean along-track line-of-sight surface velocity and u_y as the across-track mean line-of-sight surface velocity.

Including Equation (3) into the stack model can be achieved by multiplying Equation (37) from [14], where $\exp\{2\pi i \bar{\Omega}_L t_s\}$, and following the derivation of the stack model presented in [14]. The approach in Buchhaupt et al. [14] considers an arbitrary number of bursts N_b used in the SAR processing. In this study, only one burst ($N_b = 1$) is considered. The scaling of the along-track velocity of the nadir and a non-zero across-track velocity, the resulting stack model is identical to [14]. The horizontal velocity terms become:

$$v_x \mapsto \left(1 + \frac{u_x}{v_x}\right) v_x \tag{5a}$$

$$v_y \mapsto u_y \tag{5b}$$

Due to the range ambiguity of nadir-looking altimeters, across-track horizontal velocities from the left and right sides of the altimeter mostly cancel each other out and are, therefore, negligible. Therefore, in the following, only u_x is considered.

3. Implementing Horizontal Doppler Shifts in the SAR Altimetry Model

Since only u_x needs to be considered, it can be observed that u_x only reduces the along-track nadir velocity v_x, which in turn only appears as a scaling term of the slow-time $t_s \mapsto \left(1 + \frac{u_x}{v_x}\right) t_s$. All other terms are identical to [9,14]. A slow-time scaling can be implemented during the azimuth Fourier transform via linear substitution:

$$\hat{P}(f, f_D) = \frac{e^{-2\pi i \frac{f}{s} f_D}}{|1 + \frac{u_x}{v_x}|} \int_{\mathbb{R}} \hat{\hat{P}}\left(f, t_s + \tfrac{f}{s}\right) \exp\left\{-2\pi i \frac{f_D t_s}{1 + \frac{u_x}{v_x}}\right\} dt_s \tag{6}$$

where $\hat{\hat{P}}(f, t_s)$ is identical to the results from [9,14]; moreover, a small σ_v and an along-track PTR scaling error can be neglected. Additionally, the amplitude factor of $\frac{1}{|1+\frac{u_x}{v_x}|}$ leads to a small Sentinel-6MF σ_0 error of about 0.007 dB for $u_x = 10$ m/s, which is negligible. Therefore, in the following, this amplitude factor is ignored.

The power of the DDM is then calculated—after applying the slant range correction by adding a phase shift of $2\pi \frac{ch_s}{\alpha_x} \left(\frac{f_D}{2 f_c v_x}\right)^2 f + 2\pi i \frac{f_D}{s} f$ to Equation (6)—in the time-delay/Doppler frequency domain with an inverse Fourier transform:

$$\begin{aligned} P(\tau, f_D) \quad &\approx \quad \int_{\mathbb{R}} \exp\left\{2\pi i \frac{ch_s}{\alpha_x} \left(\frac{f_D}{2 f_c v_x}\right)^2 f\right\} \int_{\mathbb{R}} \hat{\hat{P}}\left(f, t_s + \tfrac{f}{s}\right) \\ &\times \quad \exp\left\{-2\pi i \frac{f_D t_s}{1 + \frac{u_x}{v_x}} + 2\pi i \tau f\right\} dt_s \, df \end{aligned} \tag{7}$$

Simply put, the line of sight velocities cause scaling of the stack sampling in the azimuth domain.

Since many optimizing algorithms run more stably and faster when the Jacobian is provided, the partial derivative of Equation (6), with respect to u_x, is given as follows:

$$\begin{aligned} \frac{\partial P(\tau, f_D)}{\partial u_x} \quad &\approx \quad \frac{v_x f_D}{(v_x + u_x)^2} \int_{\mathbb{R}} \exp\left\{2\pi i \frac{ch_s}{\alpha_x} \left(\frac{f_D}{2 f_c v_x}\right)^2 f\right\} \\ &\times \quad \int_{\mathbb{R}} 2\pi i t_s \, \hat{\hat{P}}\left(f, t_s + \tfrac{f}{s}\right) \\ &\times \quad \exp\left\{-2\pi i \frac{f_D t_s}{1 + \frac{u_x}{v_x}} + 2\pi i \tau f\right\} dt_s \, df \end{aligned} \tag{8}$$

Within the numerical retracking—such as SINCS and SINCS-OV [8,9,14]—the Fourier transforms are calculated numerically. The inverse Fourier transform from the frequency to time delay is performed via a complex to real inverse fast Fourier transform (FFT). On the other hand, a Fourier transform from equidistant slow-time values to scaled or non-equidistant Doppler frequencies is needed and, therefore, a direct FFT approach does not work. In this study, a type 2 nonuniform FFT [16] (Section 3.1) is used as it allows some shortcuts in the implementation, leading to a higher processing speed. However, a chirp Z-transform [17] is a valid alternative as well.

4. Atmospheric Refraction

In Section 2, line-of-sight velocities are mainly introduced into the SAR altimetry DDM model. However, it is important to consider another effect causing Doppler frequency scaling, namely atmospheric refraction.

It describes how objects are seen by an observer located on the sea surface. To be more precise, atmospheric refraction describes the incidence angle difference between the geometrical incidence angles $\Delta\theta_i$—associated with the travel path of light through a

vacuum—and the real incidence angle (due to refraction caused by variations in the air density). Nadir-looking instruments are given in radians, as in [18]:

$$\Delta\theta_i \approx (n-1)_{tpf}\,\frac{x}{h_s} \tag{9}$$

where $(n-1)_{tpf}$ describes the refractive modulus. The tpf subscript means that it considers the temperature, total air pressure, and water vapor pressure.

According to [19], the refractive modulus of air is given for microwave or radio-wave signals as a function of pressure P_d in the atmosphere, temperature T in degrees Celsius, and water vapor pressure P_w in the atmosphere:

$$(n-1)_{tpf} = \frac{0.000288\,P_d}{1+0.003661\,T} - \frac{0.000024\,P_w}{1+0.003661\,T} + \frac{0.005099\,P_w}{(1+0.003661\,T)^2} \tag{10}$$

The water vapor pressure is given according to [20] as follows:

$$P_w = 0.006028\,\exp\left\{\frac{17.2694\,T}{T+237.29}\right\} \tag{11}$$

It is possible to interpret atmospheric refraction as an apparent horizontal velocity—a similar mean vertical velocity observed at a specific incidence angle—with a negative sign. This means that for a scatterer, the satellite appears to be slower. The apparent horizontal velocity of the sea surface can be written as

$$v_{atm} = v_x(n-1)_{tpf} \tag{12}$$

or for Sentinel-6MF at a standard atmosphere of $P_d = 1$ atm, $T = 15$ °C, and an assumed nadir velocity of $v_x = 5940.3$ m/s of $v_{atm} = 2.2$ m/s.

Figure 3 shows the probability density of v_{atm} modeled for the Sentinel-6MF processing campaign, including cycles 017 to 051. It can be seen that the dry component of the atmosphere has a bigger contribution but most of the variation of v_{atm} is caused by the wet component.

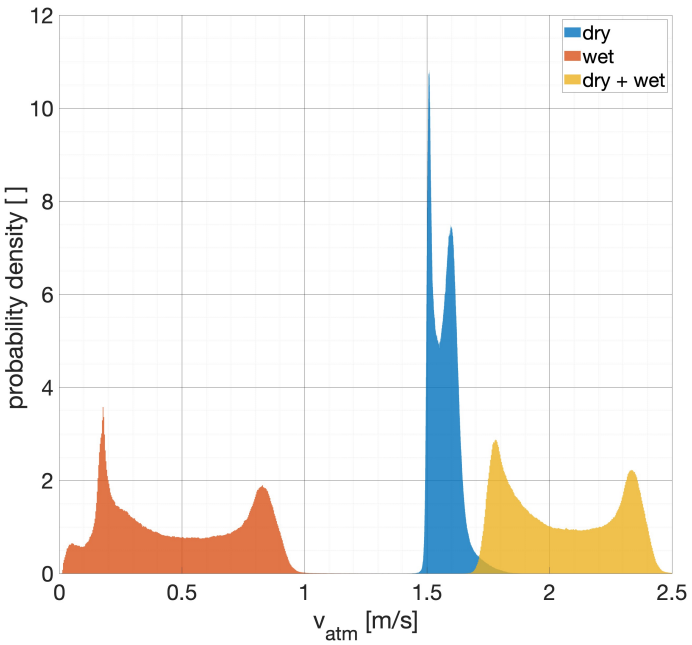

Figure 3. Probability densities of the modeled v_{atm} using ECMWF Reanalysis v5 (ERA5) sea level pressure and temperature values. The blue area denotes the dry component, the red area denotes the wet component, and the orange area denotes the total v_{atm}.

It is worth mentioning that it is possible to consider atmospheric refraction during the L1B processing by adjusting the Doppler frequency sampling if the local air pressure and the temperature at mean sea level are known. Alternatively, standard atmosphere conditions can be used to mitigate most of the atmospheric refraction. However, in this study, the L1B processing is not adjusted to include atmospheric refraction. On the other hand, it means we have to consider it when interpreting the u_x retracking results.

5. Retracking of Sentinel-6MF Signals

In order to test and validate our findings presented in the previous sections, we perform a validation campaign that encompasses one year of global Sentinel-6MF data. Additionally, Monte Carlo runs are employed to investigate the possible performance of the retracker with respect to accuracy and precision. Although the following focuses on real data processing, the simulations attempt to adopt these steps as much as feasible.

The SAR stacks were produced using the scientific LSAR-v1.1 L1A to L2 processor—being the experimental in-house processor of the Laboratory for Satellite Altimetry (LSA)—by means of an unfocused SAR processing approach, including the so-called range walk correction [21] via a chirp Z-transform. Additionally, LSAR attempts to reduce the size of the resulting DDMs by using a non-exact beam-steering approach, which results in $O_x\, N_p$ Doppler beams with equidistant Doppler frequencies per 20-Hz surface location. N_p is the number of pulses per burst and O_x is the along-track oversampling factor. Since each radar cycle consists of N_b bursts for each surface location and Doppler frequency, N_b Doppler beams occur. Since these will not provide further spatial information about the sea surface, they are averaged to one Doppler beam, resulting in an improved signal-to-noise-ratio (SNR) by a factor of $\sqrt{N_b}$. It is important to note that the zero skewness (ZSK) transform is performed before averaging the N_b Doppler beams as it only works on exponentially distributed data, and after averaging, the samples would adhere to a Gamma distribution.

During the L1B to L2 process—usually referred to as retracking—the computation of the model DDMs is performed following [8] (Section 3.3). One difference is that the computations of $F\hat{\hat{S}}SR$ and $P\hat{\hat{T}}R$ start in the f/t_s domain (contrary to the f/f_D domain, as in [8]). Therefore, a frequency vector with $N = O_t\, N_t\, N_s$ samples with a resolution of $df = \frac{f_s}{N_t N_s}$ and a slow-time vector with $M = O_x\, N_x\, N_p$ samples with a distance of $dt_s = \frac{1}{N_x f_p}$ are used for the computations. N_s is the number of samples in an echo, O_t is the oversampling factor in the time-delay domain, N_t is the receiving window-widening factor in the time-delay dimension, and N_x is the widening factor in the azimuth dimension. Mission parameters are presented in Table 1, as well as the pulse repetition frequency, which is extracted from the L1A product.

Table 1. Summary of Sentinel-6MF mission parameters used to simulate the DDMs. It is important to note that the pulse repetition frequency is not constant for Sentinel-6MF. The f_p value given here is a proxy used when simulating signals.

Symbol	Description	Value
θ_{3dBx}	Along-track half-power beamwidth	1.34°
θ_{3dBy}	Across-track half-power beamwidth	1.34°
s	Negative chirp slope	9.9748 MHz/µs
f_c	Central frequency	13.575 GHz
f_p	Pulse-repetition frequency	9100.2 Hz
f_s	Time-delay sample frequency	395 MHz
B	Usable pulse bandwidth	320 MHz
N_s	Number of samples per echo	128
N_p	Number of pulses per burst	64
k_0	Reference gate	40

The widening and oversampling parameters used in this study, are presented in Table 2.

Table 2. Sampling and window-widening parameters used in calculating the modeled Sentinel-6MF DDM.

Symbol	Description	Value
O_t	Time delay oversampling factor	2
N_t	Time delay window-widening factor	8
N_s	Number of samples per echo	128
O_x	Azimuth oversampling factor	2
N_x	Azimuth window-widening factor	4
N_b	Number of bursts per radar cycle	7
N_p	Number of pulses per burst	64

The retracking is performed with a Levenberg–Marquardt algorithm [22]. As discussed in [8], it is necessary to retrack the whole DDM to estimate σ_v, as a waveform retracker is not able to distinguish between H_s and σ_v. The same applies to u_x and t_0.

Table 3 presents an overview of the retrackers considered in this study. The abbreviation SINC stands for the signal model involving numerical convolutions. SINC2 was the first of the developed numerical retrackers and the name incorporating the PTR follows a squared sine Cardinalis function. The S in SINCS stands for SAR. OV means orbital velocity as it introduces a parameter based on the vertical component of orbital wave motions. In this study, we introduce another parameter, which mostly depends on the mean line-of-sight motions, or in other words, vertical wave-particle velocities, at a given wave slope; thus, we decided to name the new retracker SINCS-OV2, indicating two parameters that are mainly based on orbital velocities.

Table 3. Summary of retrackers used in this study.

Retracker	Mode	Input	Estimated Parameter
SINC2	LRM	waveform	A, t_0, σ_z
SINCS	SAR	waveform	A, t_0, σ_z
SINCS-OV	SAR	stack	A, t_0, σ_z, σ_v
SINCS-OV2	SAR	stack	A, t_0, σ_z, σ_v, u_x

where $\sigma_z = H_s/4$ describes the standard deviation of sea surface elevation displacements.

It is important to note that all retrackers accommodate possible negative σ_z and σ_v values—caused by noise—by setting $\sigma_z^2 \mapsto \sigma_z|\sigma_z|$ and $\sigma_v^2 \mapsto \sigma_v|\sigma_v|$. Additionally, retrackers using input signals transformed with the ZSK approach estimate the thermal noise t_n as well.

If not otherwise stated, all retrackers use a constant short-wave non-linearity factor of $\mu = 0.0546$ and a spectral narrowness parameter of $\nu = 0.39$. These values are chosen in such a way that the underlying wave spectrum is the Joint North Sea Wave Observation Project (JONSWAP) spectrum and the resulting elevation displacement skewness is $Skew[\eta] = 3\mu(1-\nu) = 0.1$.

6. Evaluating the Impact of the Mean Line-of-Sight Velocities with Monte Carlo Runs

Before beginning a real data analysis, it is important to investigate whether the new retracker SINCS-OV2 is capable of estimating bias-free geophysical parameters and what precision is achievable. Here, Monte Carlo runs of Sentinel-6MF DDMs are performed to accomplish this. As this process can be very time-consuming if all parameter combinations are simulated, some restrictions need to be set first to reduce the workload.

1. The observed surface is only affected by wind waves, ensuring that no currents or swell effects are considered.
2. The local wave field is fully developed and unidirectional, which means that it can be described by a Pierson–Moskowitz spectrum [23].
3. A standard atmosphere is assumed with $T = 15$ °C and $P = 1$ atm to simplify the implementation of v_{atm}.

Putting these restrictions into relationships with respect to H_s yields the following:

$$U_{10} = 2.1375\sqrt{g\,H_s} \tag{13a}$$

$$\sigma_v = \sqrt{\mu\,g\,\sigma_z} \tag{13b}$$

$$u_x = \sqrt{U_{10}}\cos\varphi_w + u_\star - v_{atm} \tag{13c}$$

where U_{10} describes the total wind speed ten meters above sea level. Equation (13a) results from restrictions 1 and 2, leading to a wave field described by the Pierson–Moskowitz spectrum, Equation (13b), from the definition of the short-wave non-linearity coefficient $\mu = \frac{\sigma_v^2}{g\sigma_z}$, Equation (13c) follows the findings from Section 7.2. A formulation of the friction velocity $u_\star$ is given in Equation (16).

In this study, $H_s = \{0\text{m}, 1\text{m}, 2\text{m}, 4\text{m}, 8\text{m}, 12\text{m}\}$, a short-wave non-linearity coefficient of $\mu = 0.0546$, a spectral narrowness coefficient of $\nu = 0.425$, a mean gravity acceleration of $g = 9.81$ m/s, and wind directions with respect to the satellite flight path of $\varphi_w = \{\,0.0^\circ, 22.5^\circ, \ldots 180.0^\circ\,\}$ are used for the Monte Carlo runs (negative values for φ_w are not shown here as u_x is symmetric with respect to φ_w (see Equation (13c))). For each H_s/φ_w realization, $M_{sim} = 10{,}000$ simulations are performed.

Each simulation is conducted using the following steps:

1. Compute a noise-free SINCS-OV2 DDM for current H_s/φ_w realization with arbitrary amplitude A and thermal noise of $t_n = \frac{A}{1000}$.
2. Add exponentially distributed noise to the DDM and apply the ZSK transform [8] (Equation (7.1)) to the resulting noisy DDM. Repeat this step N_b times, since in LSAR v1.1, this many Doppler beams are summed per Doppler beam. For Sentinel-6MF, $N_b = 7$.
3. Sum all N_b DDMs and normalize the result, such that the maximum power within it equals one.
4. Retrack the DDM with SINCS-OV ZSK and SINCS-OV2 ZSK.
5. Repeat all steps $M_{sim} - 1$ time for each H_s/φ_w realization.

For each H_s/φ_w realization, the mean differences, standard deviations, and correlation coefficients between the estimated parameters depending on SWH and the wind direction are calculated. Figure 4 shows the range of biases. It can be observed that SINCS-OV ZSK, given in the left plot of Figure 4, observes the SWH and wind-direction dependent bias, e.g., for $H_s = 1$ m varying from -2 mm to 9 mm. For zero SWH, a 3 mm bias can be observed, as caused by atmospheric refraction. These differences are caused by u_x—being proportional to SWH due to the restriction set in this study—leading to an azimuth scaling, which is compensated by the retracker with the range of biases. On the other hand, SINCS-OV2 ZSK is bias-free, which is a good result, as the SNR and the distribution of each sample of the DDM might lead to retracking biases.

Similar observations can be made for SWH, as given in Figure 5. SINCS-OV ZSK returns biased SWHs, varying from -0.4 cm to 3.2 cm at $H_s = 1$ m or -2.8 cm to 4.5 cm at $H_s = 12$ m. These biases are not as crucial since most SWH requirements demand an accuracy of about fifteen centimeters, but since the range estimates do not fulfill these, it would still be necessary to use SINCS-OV2 ZSK, which allows bias-free SWH estimates, except for the zero SWH, where a -9 mm bias is still present.

For σ_v given in Figure 6, similar conclusions can be drawn for SINCS-OV ZSK, showing, besides a sign change, very similar H_s/φ_w behavior. Since no accuracy requirements for altimetry results exist (the parameter is very new), no statement about the significance can be made. SINCS-OV2 ZSK allows an almost bias-free σ_v retrieval.

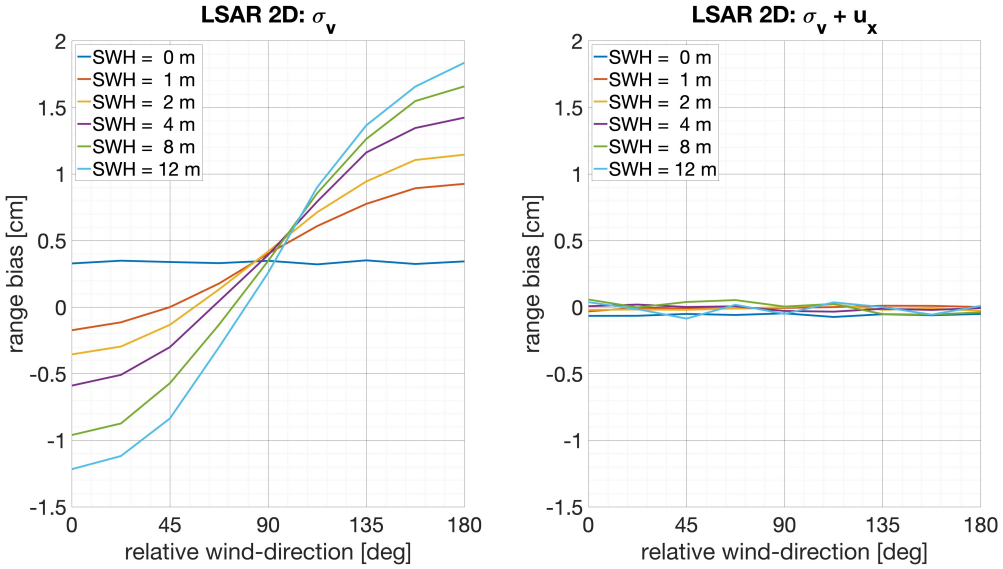

Figure 4. The Sentinel-6MF mean is measured, minus the real range, depending on the wind direction and the SWH. The given biases are retrieved from 10,000 Monte Carlo runs per SWH/wind-direction realization. The **left** plot shows the mean differences for SINCS-OV ZSK and the **right** plot shows the mean differences for SINCS-OV2 ZSK.

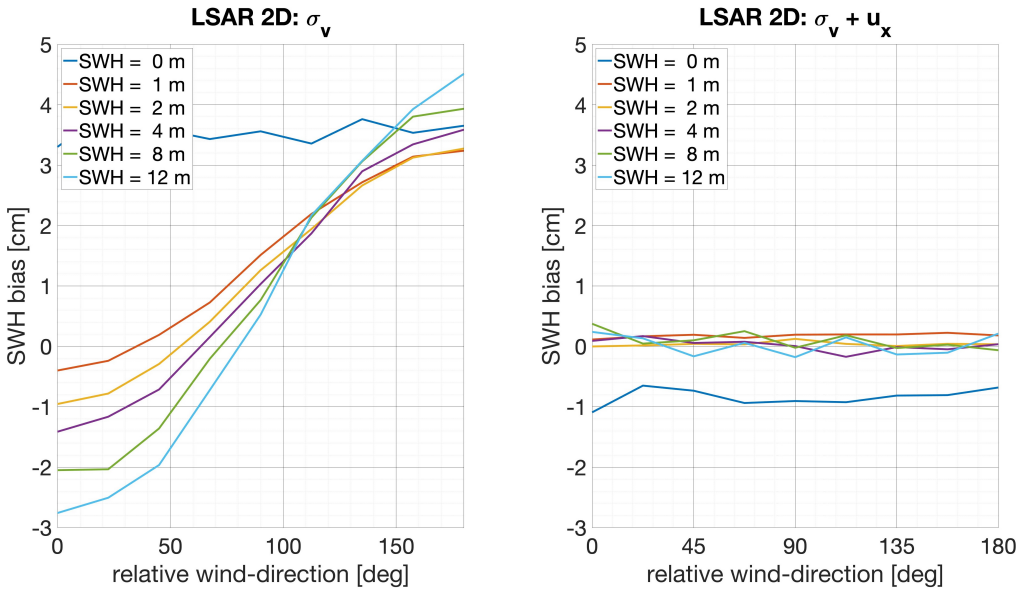

Figure 5. Sentinel-6MF mean measured minus the real SWH, depending on the wind direction and the SWH. The given biases are retrieved from 10,000 Monte Carlo runs per SWH/wind-direction realization. The **left** plot shows the mean differences for SINCS-OV ZSK and the **right** plot for SINCS-OV2 ZSK.

Since SINCS-OV ZSK does not estimate u_x, the values given in Figure 7 show u_x. SINCS-OV2 ZSK—as shown on the right plot of Figure 7—is able to estimate this new parameter bias-free.

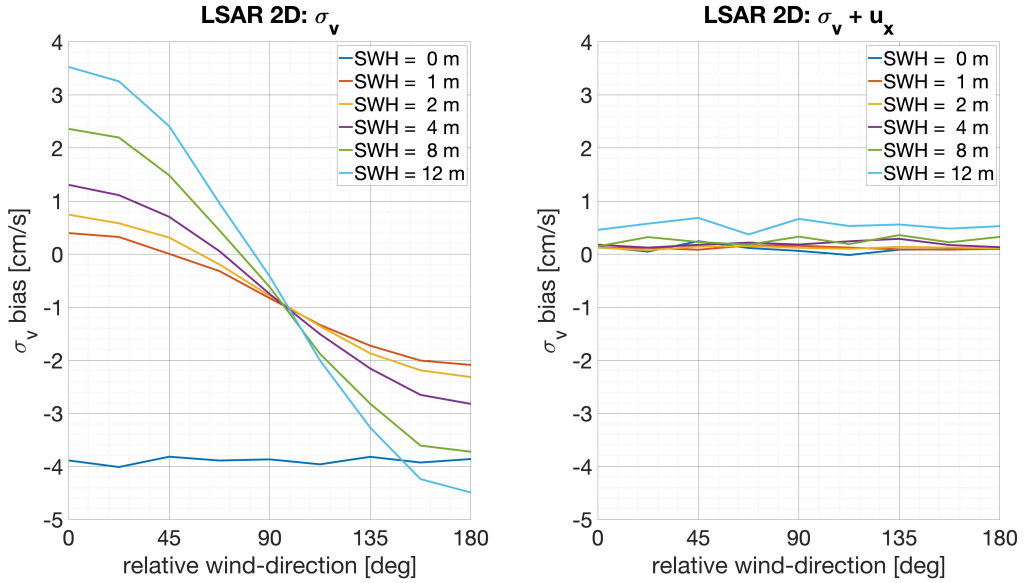

Figure 6. Sentinel-6MF mean measured minus the real σ_v, depending on the wind direction and the SWH. The given biases are retrieved from 10,000 Monte Carlo runs per SWH/wind-direction realization. The **left** plot shows the mean differences for SINCS-OV ZSK and the **right** plot for SINCS-OV2 ZSK.

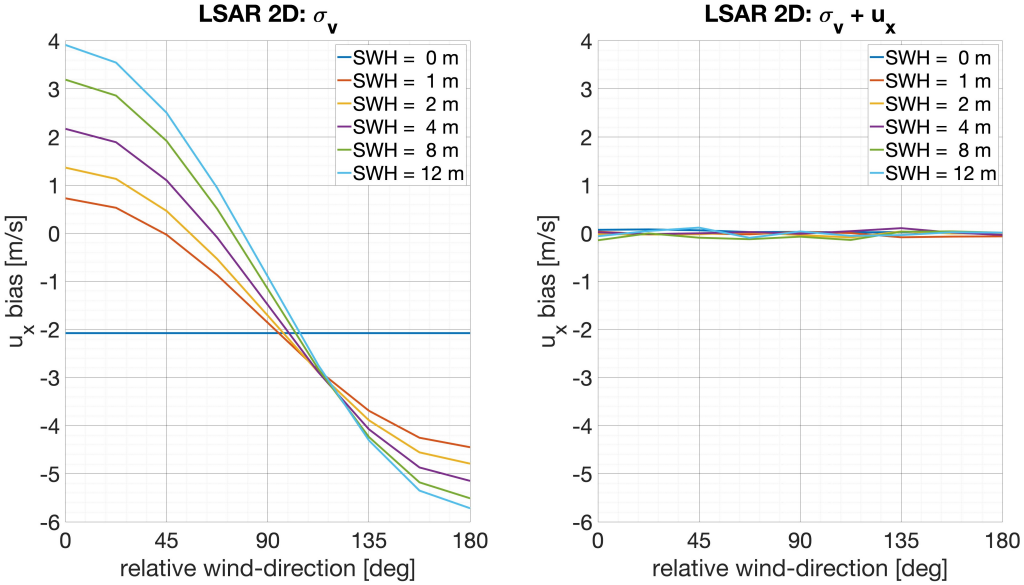

Figure 7. Sentinel-6MF mean measured minus the real u_x, depending on the wind direction and the SWH. The given biases are retrieved from 10,000 Monte Carlo runs per SWH/wind-direction realization. The **left** plot shows the mean differences for SINCS-OV ZSK and the **right** plot for SINCS-OV2 ZSK.

The standard deviations presented in Table 4 are important as they give the precision of retrieved parameters at different SWH realizations. Wind-direction dependencies were not observable and are, therefore, not shown in Table 4. The first value denotes the SINCS-OV ZSK standard deviation and the second value denotes the SINCS-OV2 ZSK standard deviation. It is observable that the retrieved precision from SINCS-OV2 ZSK is worse compared to SINCS-OV ZSK, which is no surprise since it estimates an additional parameter, u_x. This parameter is estimated with a low SNR since standard deviations are bigger than the expected values at $\varphi_w = 0°$, as given in Figure 7, degrading the precision of other parameters.

Table 4. Sentinel-6MF standard deviations for estimated parameters retrieved from 10,000 Monte Carlo runs. The first value denotes the SINCS-OV ZSK standard deviation and the second one denotes the SINCS-OV2 ZSK value.

SWH [m]	Range Std [cm]	SWH Std [cm]	σ_v Std [cm/s]	u_x Std [m/s]
0	0.8/1.3	8.6/9.8	16.8/19.5	-/2.8
1	1.1/ 1.4	2.6/3.3	6.5/7.5	-/3.6
2	1.3/1.8	2.8/3.7	6.5/7.5	-/4.2
4	1.7/2.4	3.5/5.1	7.0/8.75	-/5.4
8	2.3/3.3	5.4/8.0	9.5/11.7	-/7.2
12	2.8/4.1	7.5/9.8	12.5/14.8	-/8.7

Finally, Table 5 presents the correlation coefficients of retrieved parameters. For different SWH realizations, the values are slightly different, but for the sake of readability, only values at an SWH of two meters are presented. It can be seen that u_x is moderately to strongly correlated with other parameters; with respect to σ_v, the correlation, 0.68, is high. Additionally, the correlation coefficients of all parameters increase significantly if SINCS-OV2 ZSK is used as a retracker. The impact of this effect (and how it might be mitigated) shall be left as an open question for further study.

Table 5. Sentinel-6MF correlation coefficients for estimated parameters retrieved from 10,000 Monte Carlo runs at an SWH of two meters. The first value denotes the SINCS-OV ZSK correlation coefficients and the second one denotes the SINCS-OV2 ZSK values.

Corr(X_i,X_j)	Range	SWH	σ_v	u_x
Range	+1.00/+1.00	+0.60/+0.70	+0.18/−0.34	+0.00/−0.67
SWH	+0.60/+0.70	+1.00/+1.00	−0.26/−0.52	+0.00/−0.53
σ_v	+0.18/−0.34	−0.26/−0.52	+1.00/+1.00	+0.00/+0.68
u_x	+0.00/−0.67	+0.00/−0.53	+0.00/+0.68	+1.00/+1.00

7. Global Sentinel-6MF Data Investigation of LRM/SAR Inconsistencies

In this section, we present a comparison of LRM and SAR geophysical parameters retrieved from a global one-year processing campaign of Sentinel-6MF L1A data. In this study, cycles 017 to 051 were processed, covering a time span from 25 April 2021 to 7 April 2022. All L1A files used in this study are from processing baseline F006.

The processing was performed using our in-house experimental L1A to L2 processor, denoted as LSAR. As a reference dataset, we chose ERA5 data retrieved from the Copernicus Climate Change Service [24]. Table 6 gives the parameters which were downloaded and used in this study:

Table 6. Summary of the used ERA5 parameters. The long name here is identical to how the parameters are listed on the Copernicus Climate Data Store. The abbreviation denotes the designation of the parameter in the ERA5 network common data form (NetCDF) file. The symbol provides the usage of the parameter in this study.

Long Name	Abbr.	Symbol
Mean zero-crossing wave period	mp2	T_{02}
Significant height of combined wind waves and swell	swh	H_s
10 m eastward wind component	u10	u_{10}
10 m northward wind component	v10	v_{10}
Mean sea level pressure	msl	P
2 m temperature	t2m	T

The total wind speed U_{10}, the wind direction relative to the satellite heading φ_w, the standard deviation of vertical wave-particle velocities σ_v, and the mean line-of-sight

velocity corrected for atmospheric refraction u_x can be calculated from the parameters of Table 6 by:

$$U_{10} = \sqrt{u_{10}^2 + v_{10}^2} \tag{14a}$$

$$\varphi_w = \arctan 2(u_{10}, v_{10}) - \varphi_s \tag{14b}$$

$$\sigma_v = \frac{\pi}{2} \frac{H_s}{T_{02}} \tag{14c}$$

$$u_x = \sqrt{U_{10}} \cos \theta_w + u_\star - v_{atm} \tag{14d}$$

where φ_s is the course angle of the satellite.

We retrieved the ERA5 data at intervals of six hours.

Table 7 describes the datasets and the corresponding retracker processed for this study:

Table 7. Summary of datasets created for this study: one year of global Sentinel-6MF L1A data was processed for each dataset.

Abbr.	LRM	SAR	Note
3P	SINC2 STD	SINCS STD	As S6-MF baseline F09
3P+OV	SINC2 ZSK	SINCS-OV ZSK	As S6-MF baseline F10
3P+OV2	SINC2 ZSK	SINCS-OV2 ZSK	Estimates u_x in SAR

In the following subsections, we present how different processing approaches behave with respect to LRM/SAR discrepancies. Parameters of interest are sea level anomaly (SLA), SWH, σ_v, and u_x.

7.1. Post-Processing of Retracked Sentinel-6MF Data

Since geophysical parameters retrieved from radar altimetry data tend to be noisy, it is necessary to perform an outlier detection before the validation itself. In this study, this step is conducted on 20-Hz data.

The first step is a general threshold-based outlier detection where all values outside a defined range are replaced with not-a-number (NaN). This is conducted for all parameters, meaning that, e.g., if an SWH value is above 20 m, then all other parameters at the same surface location and epoch are set to NaN as well. Table 8 shows the valid ranges of each parameter. The values in Table 8 are selected based on the 1-Hz histograms—derived without applying an outlier detection—of each parameter, and its signal-to-noise ratio. For example, for u_x, we decided that values outside of the ± 15 m/s range should not be feasible based on its 1-Hz histogram. Additionally, we assumed a signal-to-noise ratio of about one, observing 20-Hz standard deviations. We combine this with three sigma criteria as outlier detection criteria give $\pm 15\,\mathrm{m/s} \pm 3 \times 15\,\mathrm{m/s} \mapsto \pm 60\,\mathrm{m/s}$. A similar approach was used for all other parameters besides σ_0 for which only negative values are considered as outliers.

Table 8. Summary of hard outlier thresholds.

Parameter	From	To
σ_0	0 dB	∞ dB
SLA	-3 m	3 m
H_s	-2 m	20 m
σ_v	-1 m/s	3 m/s
u_x	-60 m/s	60 m/s

The second step is a dynamic approach based on a moving median filter, which is applied to $H_s = 4\sigma_z$ and σ_v. First, a twenty-second-long moving median filter is applied to H_s (further called smoothed H_s) and afterward the same filter is applied to the absolute

difference between H_s and smoothed H_s (called smoothed absolute deviation). An outlier is detected if H_s deviates by more than six times the smoothed absolute deviation from the smoothed H_s. The same is conducted for σ_v but its absolute value is tested against six times the smoothed absolute deviation. This approach is based on a median absolute deviation-based outlier detection [25], but it uses a moving median filter and tests for four times the standard deviation. Notably, six times the median absolute deviation approximately equates to four times the standard deviation for a normally distributed parameter.

Finally, the 1-Hz data compression is straightforward, performed by averaging twenty corresponding 20-Hz data values. NaN values are ignored. If only ten values or less remain after the outlier detection, the 1-Hz value is set to NaN.

7.2. Discussion of u_x Results with Respect to ERA5

The new parameter from this study, u_x, which can only be estimated with the SINCS-OV2 ZSK retracker, does not have any requirements yet, but Table 9 shows that overall precision of this parameter is low with standard deviation values of more than one meter per second whereas mean values vary in most cases between ± 5 m/s.

Table 9. The 1-Hz u_x noise for SAR Sentinel-6MF in meters per second.

Retracker	$H_s = 1$ m	$H_s = 2$ m	$H_s = 5$ m	$H_s = 8$ m
SINCS-OV2 ZSK	1.4	1.6	2.4	2.9

From Sections 2 and 4, it can be concluded that u_x depends mainly on line-of-sight velocities caused by wave slope/vertical-velocity correlations, mean horizontal velocities, and atmospheric refraction. Nonlinear effects were not modeled in this study. In the following, we attempt to define a wind-speed-dependent formulation of u_x. To achieve this, we binned estimated 1-Hz u_x values from SINCS-OV2 ZSK retracking for different ERA5 wind speeds and directions with respect to the satellite track. For wind-speed U_{10}, central values from 0.5 m/s to 15.5 m/s with a step size of 1 m/s were chosen. For wind direction, values ranged from -175° to 175°, with a step size of 10°. An u_x value is then assigned to the nearest corresponding wind speed and wind direction. From our observations, as u_x closely follows a normal distribution, we compute the median for each wind-speed/wind-direction realization. For each wind-speed realization, we fit the resulting curve of median u_x values with the following function

$$\tilde{u}_x(U_{10}, \varphi_w) = A_{u_x}(U_{10}) \cos(\varphi_w) + b_{u_x}(U_{10}) \tag{15}$$

where A_{u_x} and b_{u_x} are estimated parameters that describe the amplitude of the directional term and a mean offset.

In the following, we present closed-form solutions for the parameters A_{u_x} and b_{u_x} and attempt to find well-established sea state parameters, e.g., in this study, the friction velocity $u_\star$ for b_{u_x}. However, we do not claim that b_{u_x} equals $u_\star$. We only observe that both parameters show very similar wind-speed behaviors.

Figure 8 provides the A_{u_x} (left plot) and b_{u_x} (right plot) estimates for the given ERA5 wind speeds. The left plot shows that the directional amplitude A_{u_x} can be described—with an error of about 10%—by the square root of the wind speed U_{10}. The corresponding geophysical parameter is $a_{vx}\frac{\sigma_v}{\sigma_x}$, approximately describing the ratio between the slope/velocity covariance and the along-track wave slope variance [9]. The right plot provides the offset parameter b_{u_x} with respect to the ERA5 wind speed U_{10}. The red curve denotes the friction velocity computed with U_{10}, as described in Edson et al. [26]; Figure 10 shows good agreement with b_{u_x}.

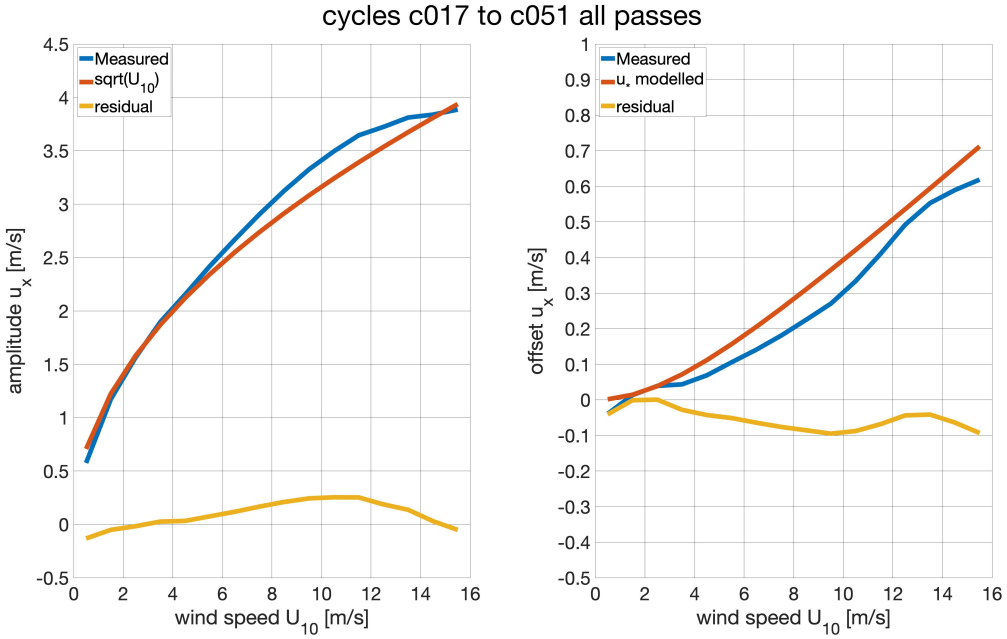

Figure 8. Best parameters to fit u_x as a cosine function, plus a constant for different wind speeds. The atmospheric refraction considered here accounts for varying air pressure and temperature variations at the mean sea level. (**Left**): The amplitude of the cosine. Blue denotes the measured value, red denotes the square root of the wind speed that is ten meters above sea level, and orange denotes the difference between blue and red. (**Right**): The offset parameter. Blue denotes the measured value, red denotes the friction velocity modeled according to Edson et al. [26] (Figure 10), and orange denotes the difference between blue and red.

A detailed formulation of the computation of $u_\star$ from the wind wave spectra at high wind speeds is given in Takagaki et al. [27]. In this study, we used a simpler formulation derived in Edson et al. [26], which describes $u_\star$ as a linear function of U_{10} for three different wind speed cases. However, we fit the formula given by Edson et al. [26] with a hyperbola:

$$u_\star \approx \sqrt{(0.2923\,\mathrm{m/s})^2 + (0.062\,U_{10})^2} - 0.2923\,\mathrm{m/s} \tag{16}$$

This representation leads to a good match with b_{u_x}.

In Figure 9, we present a map of smoothed u_x estimates derived from ascending and descending passes from cycles 017 to 051. On the top and bottom plots, the geographical features of u_x are well observable, especially in the northwest of South America and the west of Africa. Additionally, it can be seen that u_x results from ascending and descending passes, with different signs at latitudes between $\pm 45°$. Outside these latitudes, the signs are mostly identical due to similar course angles in these regions.

Another interesting piece of information is the variation of u_x in different regions. To present this—as shown in Figure 10—we estimated the standard deviation of u_x over cycles to describe the variation over time. Since u_x follows a normal distribution, here, the standard deviation is estimated as $1.4826\,MAD(u_x)$ to make the map more robust with respect to extreme events or outliers. Interestingly, the variation does not differ much between ascending and descending passes. Additionally, the standard deviations at latitudes between $\pm 30°$ are low in areas where u_x is in terms of a big amount. Outside these latitudes, the standard deviations are high in areas with large means, u_x.

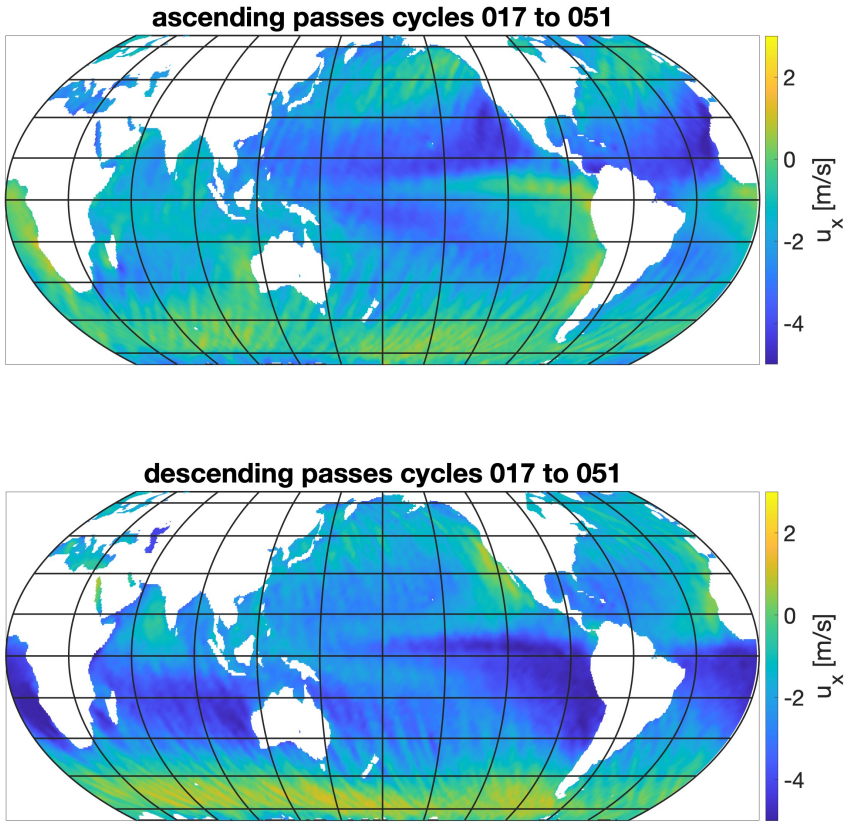

Figure 9. Average map over all cycles of u_x—not corrected for atmospheric refraction—retrieved from Sentinel-6MF SAR stacks.

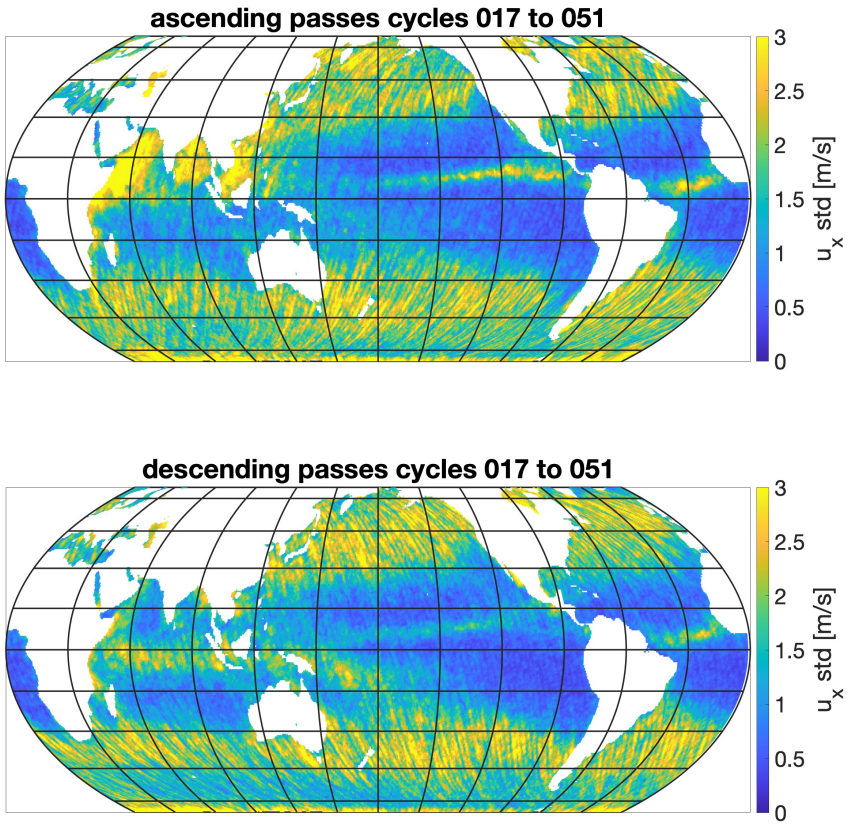

Figure 10. Standard deviation map over all cycles of u_x—not corrected for atmospheric refraction—retrieved from Sentinel-6MF SAR stacks.

Figure 11 shows the difference between the mean u_x as shown in Figure 9 and the mean u_x calculated with ERA5 data. It can be seen that the differences vary between ± 1 m/s and the relative error is usually within 10%. However, we cannot state if the remaining errors are within ERA5 wind speed data or if it is necessary to include currents and swell to improve the match. Nevertheless, the results are quite promising and model u_x seems to match the measured u_x well enough to be used as an input parameter for a lookup table (LUT).

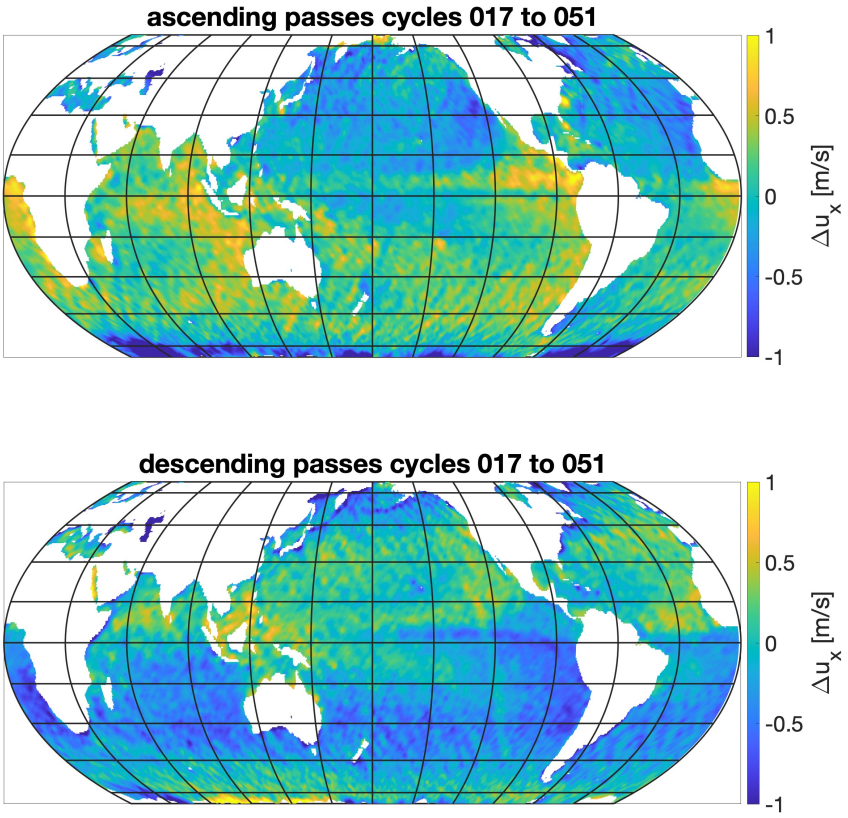

Figure 11. Average map over all cycles of the difference between u_x resulting from the Sentinel-6MF stack retracking and u_x modeled from ERA5 data.

To conclude this subsection, it can be stated that with u_x, a new geophysical parameter can be estimated from SAR stacks. Due to u_x mainly depending on the wind speed and direction, it opens up the possibility of estimating directional winds from SAR altimetry.

7.3. Discussion of SAR σ_v Results

Due to the fact that LRM is unaffected by vertical wave-particle velocities, it is not possible to estimate σ_v by retracking LRM waveforms. Therefore, no comparison between SAR and LRM σ_v could be performed. As this parameter is quite new, we could not find accuracy or noise requirements for it. However, we still provide the 1-Hz standard deviation of SAR σ_v in Table 10. The main observation from Table 10 is the worse precision of SINCS-OV2 ZSK compared to SINCS-OV ZSK, which is hinted at in Tables 4 and 5, indicating that u_x/σ_v correlations in the retracking significantly reduce the precision of σ_v.

Table 10. The 1-Hz σ_v noise for SAR Sentinel-6MF in centimeters per second.

Retracker	$H_s = 1$ m	$H_s = 2$ m	$H_s = 5$ m	$H_s = 8$ m
SINCS-OV ZSK	8.5	9.2	12.3	17.2
SINCS-OV2 ZSK	13.2	14.2	20.4	28.6

As no differences between ascending and descending passes could be observed for the mean σ_v or the standard deviation of σ_v, Figure 12 shows only ascending passes. The upper plot presents the mean overall cycles and the lower plot presents the standard deviation. Both show results retrieved with the SINCS-OV2 ZSK SAR retracker. Comparing the upper plot of Figure 12 with Figure 9, no similarities can be seen. This is probably caused by the fact that u_x depends on the wind direction and σ_v does not.

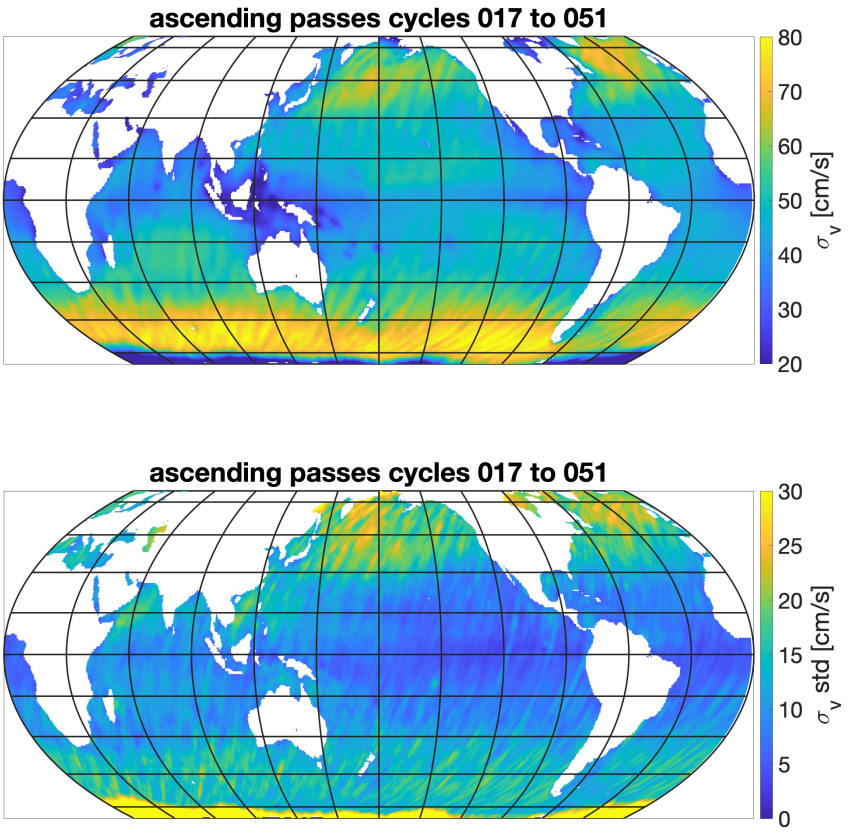

Figure 12. Average map over all cycles of σ_v—not corrected for the attenuation factor a_v—retrieved from Sentinel-6MF SAR stacks using the SINCS-OV2 ZSK retracker.

On the other hand, when comparing σ_v from SINCS-OV2 ZSK and σ_v from SINCS-OV ZSK, as shown in Figure 13, a clear resemblance with Figure 9 showing u_x is observable. This leads to the conclusion that σ_v estimates are affected by u_x as well, but the magnitude is less than ten centimeters and only a few percentage points of σ_v.

Overall, it can be stated that the impact of u_x on σ_v is a few percentage points and, therefore, is rather small.

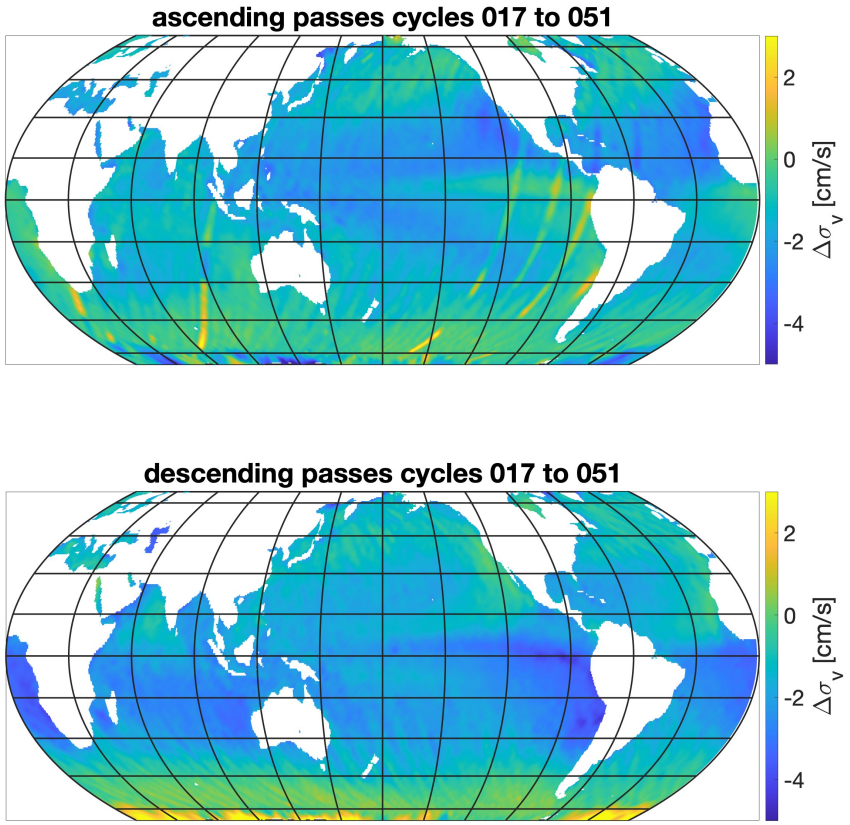

Figure 13. Average map over all cycles of differences between σ_v retrieved using the SINCS-OV2 ZSK retracker and σ_v retrieved using the SINCS-OV ZSK retracker. Both are not corrected for the attenuation factor a_v and are retrieved from Sentinel-6MF SAR stacks.

7.4. Discussion of LRM/SAR SLA Discrepancies

SLA is the most important parameter in radar altimetry for ocean applications as it provides crucial information about the sea level rise and local events, such as storms/hurricanes and currents. Therefore, mission requirements regarding these parameters are rather strict, requiring range estimate accuracies in the centimeter range.

Table 11 presents the range noise upper limits for LRM and the achieved 1-Hz standard deviations of SLA measurements. The value for $H_s = 2$ m is a mission requirement. It can be observed that SINCS2 STD and SINC2 ZSK both reach the upper limits and the mission requirement for SWH values above two meters. For the one-meter case, they are 1.25 cm above the 1.2 cm requirement. Additionally, we note that SINC2 ZSK has slightly better precision than SINC2 STD. Additionally, it is worth mentioning that there is a goal for 1.0 cm at $H_s = 2$ m, which SINC2 ZSK makes progress toward.

Table 11. The 1-Hz SLA noise for LRM Sentinel-6MF in centimeters.

Retracker	$H_s = 1$ m	$H_s = 2$ m	$H_s = 5$ m	$H_s = 8$ m
Requirement	1.20	1.50	2.40	3.20
SINC2 STD	1.25	1.40	1.82	2.02
SINC2 ZSK	1.25	1.35	1.70	1.95

For the SAR mode, the SLA standard deviations are presented in Table 12. SINCS STD, which will be implemented in Sentinel-6MF baseline F09, does not fulfill the eight-meter SWH requirements of 2.00 cm as it is 10% bigger. On the other hand, SINCS-OV ZSK performs better at high sea states and it reaches the $H_s = 8$ m requirement with a value of 1.86 cm. SINCS-OV2 ZSK—estimating additionally u_x—performs worse for small to

medium sea states, but almost reaches the high sea state's upper noise limit by exceeding the value by 1%.

Table 12. The 1-Hz SLA noise for SAR Sentinel-6MF in centimeters.

Retracker	$H_s = 1$ m	$H_s = 2$ m	$H_s = 5$ m	$H_s = 8$ m
Requirement	0.70	0.80	1.30	2.00
SINCS STD	0.45	0.60	1.22	2.22
SINCS-OV ZSK	0.45	0.56	1.11	1.86
SINCS-OV2 ZSK	0.56	0.70	1.25	2.02

However, the accuracy of an estimated parameter, which is more important than the precision discussed before, is usually described by the root-mean-square error (RMSE). In the following, we will focus on mean differences between LRM and SAR with respect to ERA5 SWH and u_x.

Table 13 provides the main statistics of this section for all three datasets. The slope and offset denote the linear regression parameter, median denotes the median of the SAR/LRM SLA differences, STDD denotes the standard deviation of differences (STDD), and NP denotes the number of points. The 3P dataset representing SINCS STD for SAR and SINC2 STD for LRM shows the highest dependency on SLA differences with u_x, with a regression slope of -0.277 cm/(m/s), the highest offset (6.3 mm), median (11.1 mm), and STDD (19.3 mm). Surprisingly, the 3P+OV dataset—using ZSK transforms and a vertical velocity tracker—shows better performance with a significantly lower offset (1.5 mm), median (5.7 mm), and STDD (17.0 mm), but the u_x dependency has a regression slope of -0.253 cm/(m/s) that is almost unchanged compared to the 3P dataset. By far, the best agreement between SAR and LRM is reached with the 3P+OV2 dataset, which estimates additionally u_x in SAR, with an insignificant slope of 0.007 cm/(m/s), an offset of 1.4mm, a median of differences of 1.2 mm, and an STDD of 16.8 mm. Therefore, SINCS-OV2 ZSK eliminates the u_x dependency.

Table 13. Regression of SAR minus LRM 1-Hz SLA values with respect to u_x. The slope is given in cm/(m/s). Offset, median, and STDD in centimeters.

Abbr.	Slope	Offset	Median	STDD	NP
3P	-0.277	0.63	1.11	1.93	16,474,989
3P+OV	-0.253	0.15	0.57	1.70	16,674,069
3P+OV2	0.007	0.14	0.12	1.68	16,571,956

The following figures provide a visualization of Table 13.

As indicated by Figure 14, the mean differences between the SAR and LRM SSH estimates—retrieved from the SINCS STD SAR waveform retracker and SINC2 STD LRM retracker—look very similar compared to Figure 9, showing mean u_x values. The mean differences are over two centimeters, which does not fulfill the mission requirements.

The same can be stated about Figure 15 showing the standard deviations over all cycles as it looks very similar to Figure 10, where the u_x standard deviation is presented. Figure 15 shows that the variations in mean SSH differences between SINCS STD and SINC2 STD vary between two and ten millimeters. As in Figure 10, at latitudes between $\pm 45^\circ$, the standard deviations are low when the mean differences are big, and outside this region, the standard deviations become bigger if the mean increases.

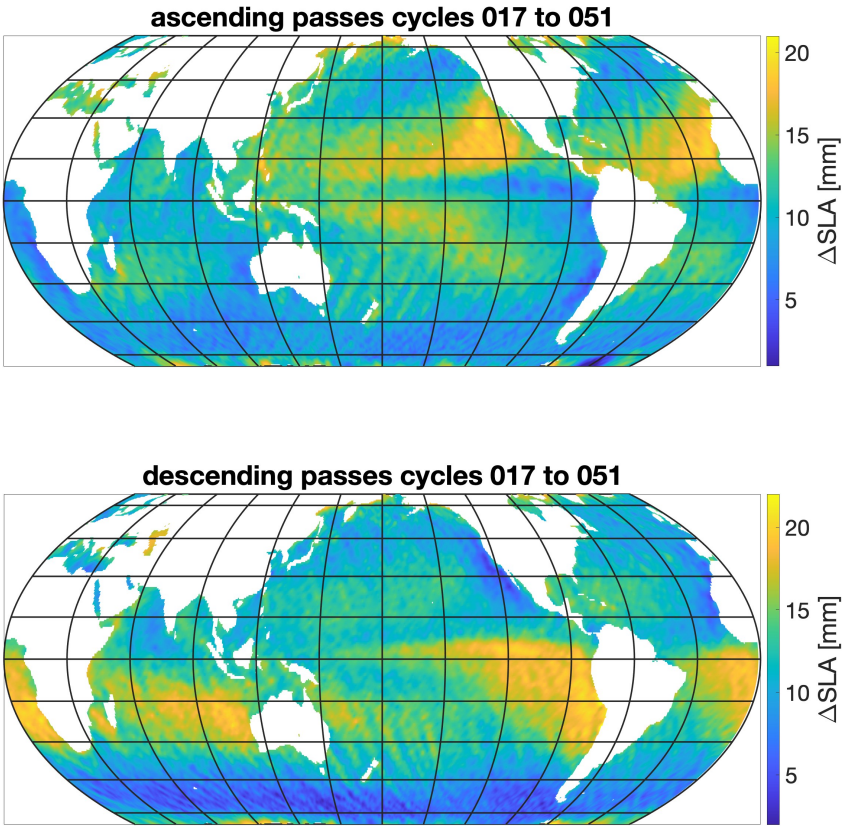

Figure 14. Average map over all cycles of differences between SSH retrieved using the SINCS STD SAR retracker andSSH retrieved using the SINC2 STD LRM retracker.

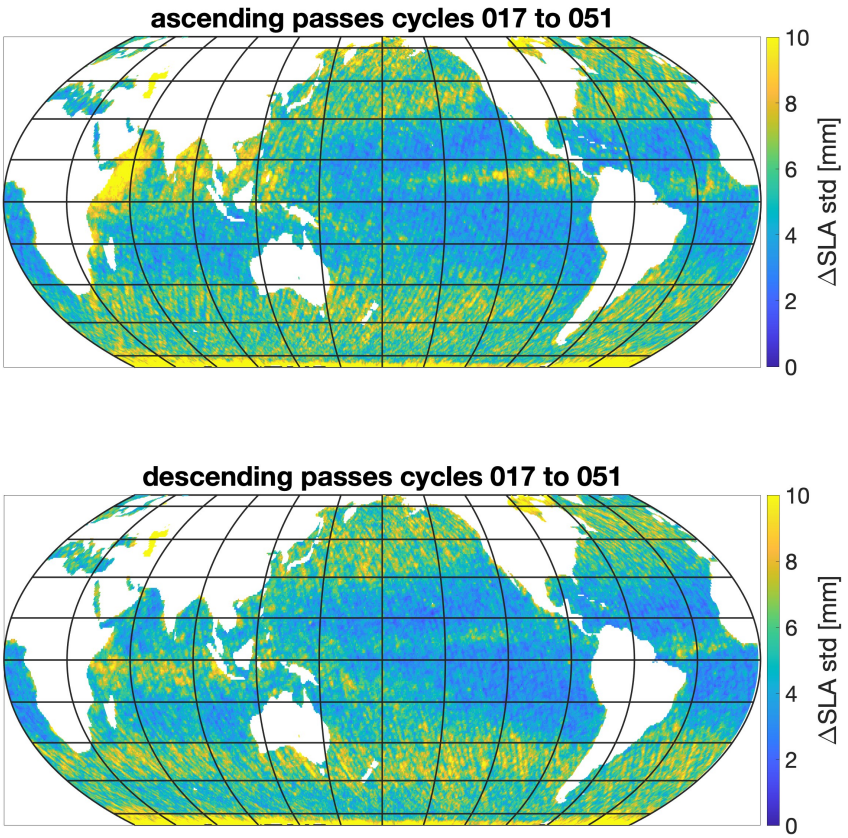

Figure 15. Map of standard deviations over all cycles of differences between SSH retrieved using the SINC2 STD LRM retracker and SSH retrieved using the SINCS STD SAR retracker.

Figure 16 shows the mean differences over all cycles between SAR and LRM for the 3P+OV2 dataset, which estimates u_x as well. It can be observed that no obvious SSH inconsistencies exist between SAR and LRM besides a bias of 1.4 mm, as shown in Table 13. Ascending and descending passes show the same behavior as no differences can be observed.

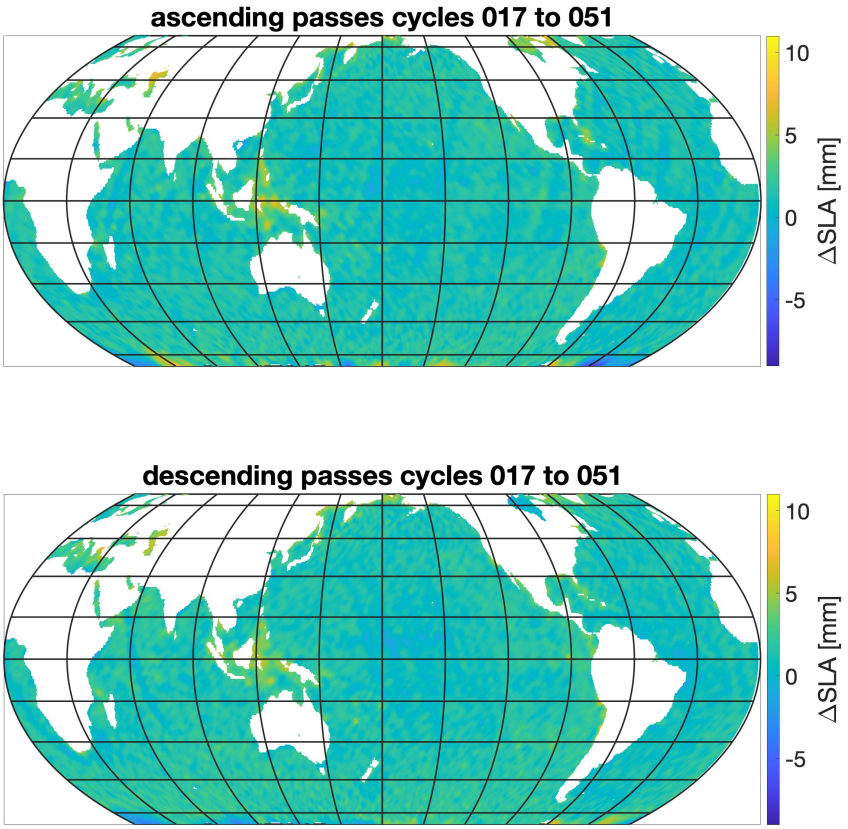

Figure 16. Average map over all cycles of differences between SSH retrieved using the SINCS-OV2 ZSK SAR retracker andSSH retrieved using the SINCS2 ZSK LRM retracker.

The same can be stated about the standard deviations of the 3P+OV2 dataset shown in Figure 17 since no significant regional characteristics are observable. In coastal regions or typical sea ice regions, the standard deviations are, in most cases, about 2.6 mm. This is an important result as it indicates that no spatial behavior of SSH discrepancies between SAR and LRM exist when applying the same processing steps, as in the 3P+OV2 dataset.

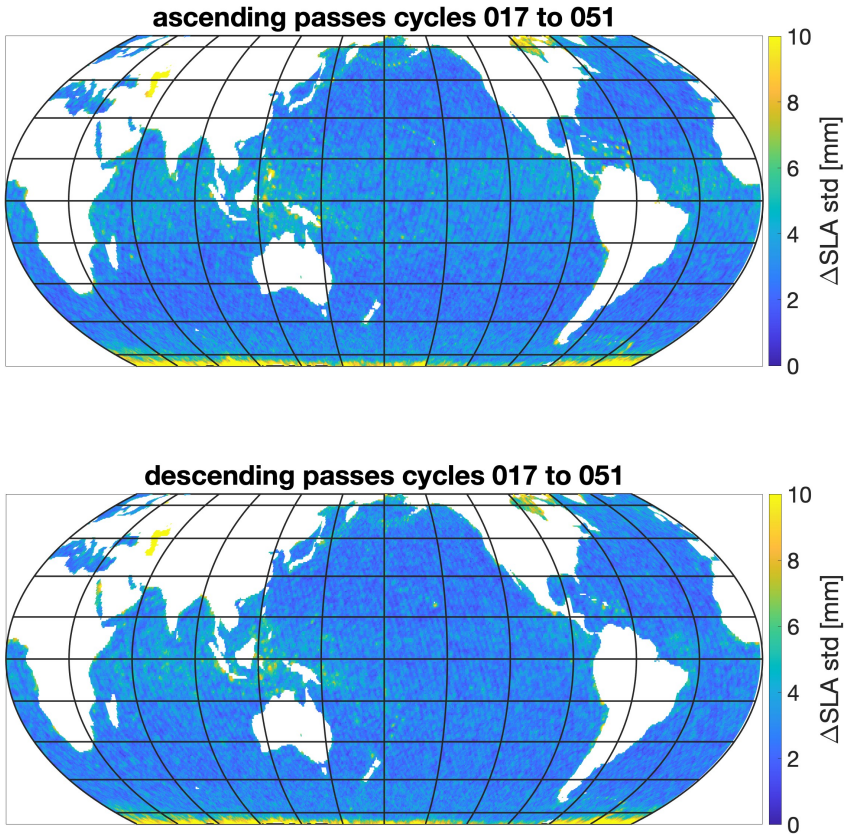

Figure 17. Map of standard deviations over all cycles of differences between SSH retrieved using the SINC2 ZSK LRM retracker andSSH retrieved using the SINCS-OV2 ZSK SAR retracker.

7.5. Discussion of LRM/SAR SWH Discrepancies

Near-real-time wave heights are critical parameters for end users for navigation and safety. However, requirements are based on user requirements and an estimate of a combination of noise and systematic errors. The goal is to reduce systematic errors to 10 cm for SWH between 0.5 and 8 m. For Sentinel-6MF, an accuracy requirement of 15 cm $\pm$ 5% SWH is defined. With a current state-of-the-art SAR retracker, this requirement is not possible to achieve due to vertical wave-particle velocities affecting SAR SWH estimates. However, in LRM, these requirements are achievable due to the incoherent processing vertical velocities not impacting LRM, as shown in Table 14. It is worth mentioning that the ZSK transform significantly improves the precision of SWH estimates by halving standard deviations.

Table 14. The 1-Hz SWH noise for LRM Sentinel-6MF in centimeters.

Retracker	$H_s = 1$ m	$H_s = 2$ m	$H_s = 5$ m	$H_s = 8$ m
SINC2 STD	9.0	9.2	11.2	13.2
SINC2 ZSK	4.9	4.9	6.0	7.3

Table 15 denotes the standard deviations of 1-Hz SWH SAR estimates. Again, these values are not meaningful for SINCS STD as they do not consider σ_v causing large SWH biases. Even so, SINCS-OV ZSK and SINCS-OV2 ZSK estimate additional wave velocity parameters, and the 1-Hz standard deviations are significantly lower for SINCS STD.

Table 15. The 1-Hz SWH noise for SAR Sentinel-6MF in centimeters.

Retracker	$H_s = 1$ m	$H_s = 2$ m	$H_s = 5$ m	$H_s = 8$ m
SINCS STD	3.8	4.2	8.1	14.2
SINCS-OV ZSK	2.2	2.9	6.1	11.0
SINCS-OV2 ZSK	2.7	3.2	6.3	11.2

Table 16 shows the statistics of the linear regression of SAR/LRM 1-Hz SWH differences with respect to u_x. It is important to note that least square method-based linear regressions assume normally distributed variables, which is not the case for SWH, which approximately follows a Rayleigh distribution. Therefore, the results presented in Table 16 should not be over-interpreted. However, they provide insight into potential u_x dependencies.

Table 16. Regression of SAR minus LRM 1-Hz SWH values with respect to u_x. The slope is given in cm/(m/s). Offset, median, and STDD in centimeters.

#	Slope	Offset	Median	STDD	NP
3P	2.345	35.2	30.9	15.2	16,858,661
3P+OV	0.568	−1.4	−2.4	5.3	16,797,917
3P+OV2	−0.166	−1.5	−1.1	5.4	16,693,252

The SINCS retracker used in the 3P dataset in Table 16 does not consider vertical velocities and, therefore, SINCS STD has bad agreement with SINC2 STD. On the other hand, the 3P+OV dataset—including σ_v as a free parameter—already provides very good agreement with an offset of −1.4 cm, median differences of −2.4 cm, and STDD of 5.3 cm. The regression slope of 0.568 cm/(m/s) points toward a small u_x dependency. However, the resulting biases are always below the accuracy requirement of 15 cm ± 5% SWH. The 3P+OV2 dataset performs similar to the 3P+OV dataset. The only noticeable differences are the lower median of differences of −1.1 cm and the small u_x dependency causing a regression slope of −0.166 cm/(m/s).

Figure 18 visualizes the mean SWH differences over all cycles between SAR and LRM, or in other words, from the 3P dataset. It can be observed that ascending and descending passes behave similarly, which is no surprise as these differences are mostly caused by vertical wave-particle velocities. Therefore, Figure 18 shows very similar behavior to Figure 12, given the average σ_v values. A more detailed discussion about the effect of σ_v on SWH is given for CryoSat-2 in Buchhaupt [8] and Buchhaupt et al. [9]. Overall, for Sentinel-6MF, the discrepancies in SWH between the SAR waveform retracker and LRM waveform retracker exceed the accuracy requirements of 15 cm at two-meter SWH, as well as the goal of 10 cm at two-meter SWH.

On the other hand, for the 3P+OV dataset, considering vertical wave-particle velocities by estimating σ_v, the mean SWH differences between SAR and LRM, as given in Figure 19, become much smaller compared to the 3P dataset. The remaining differences show the same behavior as u_x, visualized in Figure 9, and indicated in Table 16.

Introducing the Doppler frequency scaling—by introducing u_x as an estimated parameter, such as in the 3P+OV2 dataset—further reduces the SWH differences between SAR and LRM averaged over all cycles. As shown in Figure 20, ascending and descending passes behave similarly, and for latitudes between ±30°, the SWH is very small. However, a latitude dependency is observable, which increases with the absolute latitude. It is still not clear what causes this issue, but overall, SWH derived from SAR and LRM has very good consistency in the 3P+OV2 dataset, which includes σ_v and u_x.

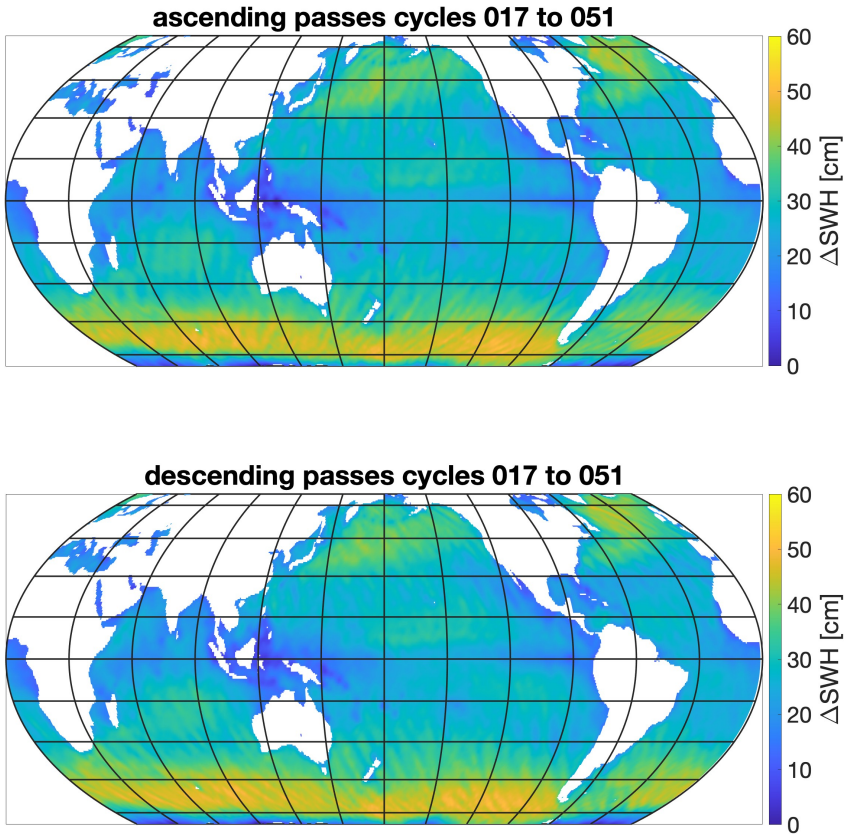

Figure 18. Average map across all cycles showing differences in SWH, retrieved using the SINCS STD SAR retracker, and SWH, retrieved using the SINC2 STD LRM retracker.

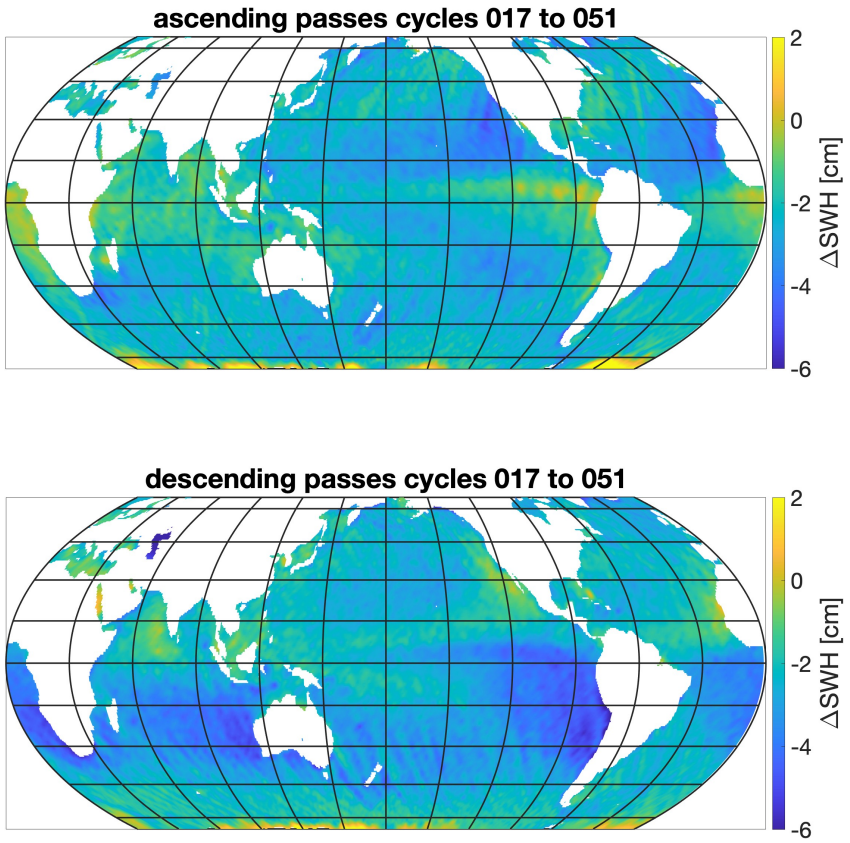

Figure 19. Average map over all cycles of differences between SWH retrieved using the SINCS-OV ZSK SAR retracker and SWH retrieved using the SINC2 ZSK LRM retracker.

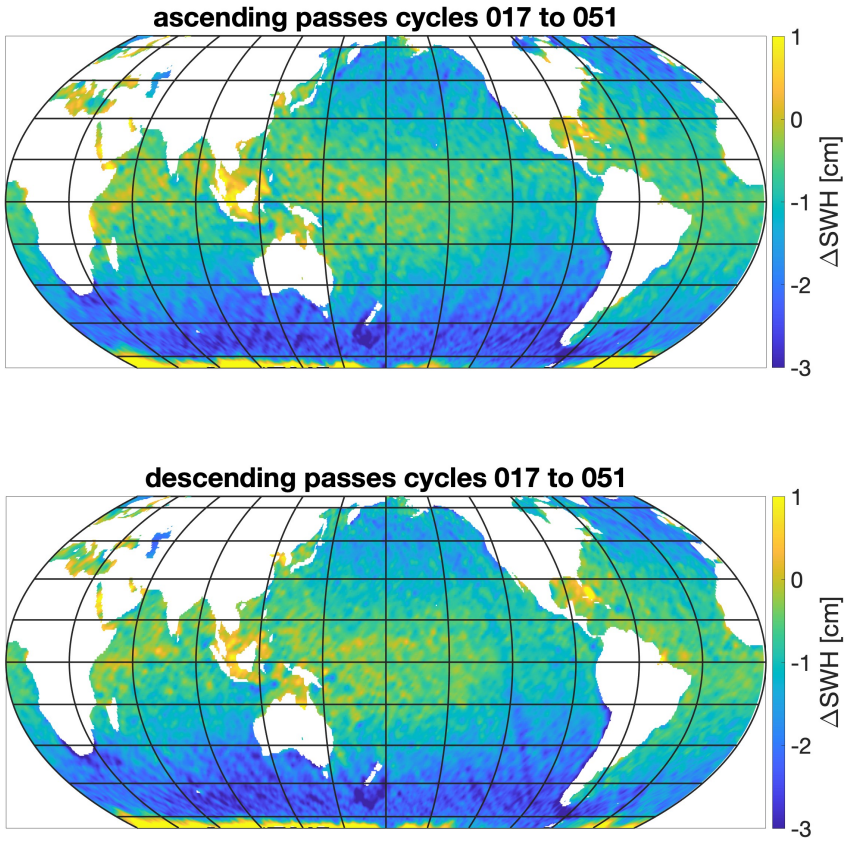

Figure 20. Average map over all cycles of differences between SWH retrieved using the SINCS-OV2 ZSK SAR retracker and SWH retrieved using the SINC2 ZSK LRM retracker.

8. Conclusions

In this study, we introduce a new SAR stack retracker called SINCS-OV2 ZSK, which provides SSH and SWH estimates with very good agreement, with respect to LRM results. It estimates a novel parameter u_x, which acts like a horizontal along-track sea surface motion and leads to a Doppler frequency scaling. Moreover, we show that the Doppler frequency scaling is caused by:

- Line-of-sight wave motion: This is mostly caused by vertical velocities observed at a given incidence angle of the electromagnetic wave. This depends on the wind speed and wind direction. Usually between ± 5 m/s.
- Atmospheric refraction: This is caused by different refractive indices at the satellite position and the observed sea surface. This depends on the dry air pressure at sea level and water vapor content at sea level, usually between -2.5 m/s and -1.7 m/s.
- Swell and currents: This was not investigated in this study, which focused on wind waves. We plan to consider swell waves and currents in a later study.

We performed Monte Carlo runs to verify that the newly presented retracker approach provides bias-free estimates and showed that not considering u_x in the retracking leads to significant SSH biases up to several centimeters. On the other hand, SWH and the standard deviation of vertical wave-particle velocities σ_v are less affected by biases in the order of a few percentage points. By introducing u_x as a free parameter within a SAR stack retracker—such as SINCS-OV2 ZSK—we managed to eliminate almost all of the discrepancies between LRM and SAR altimetry retracking results.

Additionally, we find a formulation to describe u_x as a function of eastward and northward wind components from the ERA5 model. This is important as this formulation can be used to build lookup tables to consider SSH biases, e.g., for Copernicus Sentinel-6 data provided by EUMETSAT, which does not consider u_x during the retracking.

Of course, if it is possible to estimate u_x from eastward and northward wind components, it should be possible to retrieve estimates of eastward and northward wind components from u_x retracking results via SAR altimetry. Therefore, the SINCS-OV2 ZSK retracker opens the door to obtaining directional information about wind fields.

In further studies, we plan to investigate other SAR altimetry missions, such as Sentinel-3, to verify the results found here. Additionally, we plan to investigate the effects caused by swell waves and currents.

Author Contributions: Writing—original draft preparation, C.K.B.; conceptualization, C.K.B. and A.E.; writing—review and editing, D.V., W.H.F.S., L.F. and E.L. All authors have read and agreed to the published version of the manuscript.

Funding: This research was supported by the NOAA component of the NASA-NOAA Joint program announced in NRA NNH20ZDA001N-OSTST: Ocean Surface Topography Science Team; Project/Proposal title: "Towards an Improved Reconciliation of High- and Low-Resolution Ocean Altimeter Measurements Under Changing Surface Wave Structure Conditions", PI. Egido, and by the NOAA Product Development, Readiness, and Application (PDRA)/Jason Program. It was also supported by NOAA grant NA19NES4320002 (Cooperative Institute for Satellite Earth System Studies—CISESS) at the University of Maryland/ESSIC. Additionally, part of this work was supported by ST13301CQ0050 1332KP22FNEED0042 via the Ocean Surface Topography Science Team support.

Data Availability Statement: The data presented in this study are available on request from the corresponding author.

Acknowledgments: The scientific results and conclusions, as well as any views or opinions expressed herein, are those of the author(s) and do not necessarily reflect the views of NOAA or the Department of Commerce.

Conflicts of Interest: The authors declare no conflicts of interest.

Appendix A. Flat Sea Surface Response

The FSSR representation in the frequency/slow-time domain is according to [14] (Equation (52)), calculated by assuming a Gaussian antenna pattern [28] with parameters a and b, given as

$$a = \frac{\sqrt{\ln 2}}{\sin(\theta_{3dBx}/2)} \tag{A1a}$$

$$b = \frac{\sqrt{\ln 2}}{\sin(\theta_{3dBy}/2)} \tag{A1b}$$

where θ_{3dBx} is the along-track and θ_{3dBy} is the across-track half-power antenna beam width.

The final representation is given as

$$\hat{FSSR}(f, t_s) = \frac{A}{\sqrt{s_x\, s_y - s_{xy}^2}} \exp\left\{ \frac{s_y\, \zeta_x^2 + s_x\, \zeta_y^2 + 2\zeta_x\, \zeta_y\, s_{xy}}{s_x\, s_y - s_{xy}^2} \right\} \tag{A2}$$

where the amplitude A is given as

$$\begin{aligned} A &= \frac{G_0^2\, \sigma_0\, \lambda_c^2\, c}{4(4\pi)^2 \sqrt{\alpha_x \alpha_y} L_p L_{RX} h_s^3} \exp\left\{ -\alpha_0 \frac{x_s^2 + y_s^2}{h_s^2} \right\} \\ &\times \exp\left\{ -2\frac{\Delta x^2}{h_s^2} \left[a^2 \cos^2 \xi_y + b^2 \sin^2 \xi_y \right] \right\} \\ &\times \exp\left\{ -2\frac{\Delta y^2}{h_s^2} \left[b^2 \cos^2 \xi_y + a^2 \sin^2 \xi_y \right] \right\} \end{aligned} \tag{A3}$$

Additionally, s_x, s_y, and s_{xy} describe the behaviors of the stack in the range dimension, given by

$$s_x = \delta_x + \frac{c}{\alpha_x h_s}\alpha_0 + 2\pi i f \tag{A4a}$$

$$s_y = \delta_y + \frac{c}{\alpha_y h_s}\alpha_0 + 2\pi i f \tag{A4b}$$

$$s_{xy} = \delta_{xy} + 2\pi i \frac{\alpha_{xy}}{\sqrt{\alpha_x \alpha_y}} f \tag{A4c}$$

where δ_x, δ_y, and δ_{xy} are auxiliary parameters that mainly depend on the antenna characteristics. They are given by

$$\delta_x = 2\frac{c}{\alpha_x h_s}\left[a^2 \cos^2 \xi_y + b^2 \sin^2 \xi_y\right] \tag{A5a}$$

$$\delta_y = 2\frac{c}{\alpha_y h_s}\left[b^2 \cos^2 \xi_y + a^2 \sin^2 \xi_y\right] \tag{A5b}$$

$$\delta_{xy} = 2\frac{c}{\sqrt{\alpha_x \alpha_y} h_s}\left[a^2 - b^2\right] \sin(2\xi_y) \tag{A5c}$$

where ξ_r is the roll angle, ξ_p is the pitch angle, and ξ_y is the yaw angle of the antenna.

On the other hand, ζ_x and ζ_y describe the stack behaviors in azimuth or along-track dimensions and antenna mispointing. Due to the shift of $t_s \mapsto t_s + \frac{f}{s}$, they slightly differ from [14] (Equation (53)) and are given here as

$$\zeta_x = \beta_x + \sqrt{\frac{c}{\alpha_x h_s}}\frac{x_s}{h_s}\alpha_0 - 2\pi i \sqrt{\frac{\alpha_x}{c h_s}} f_c v_x t_s \tag{A6a}$$

$$\zeta_y = \beta_y + \sqrt{\frac{c}{\alpha_y h_s}}\frac{y_s}{h_s}\alpha_0 + 2\pi i \sqrt{\frac{\alpha_x}{c h_s}}\frac{\alpha_{xy}}{\sqrt{\alpha_x \alpha_y}} f_c v_x t_s \tag{A6b}$$

where auxiliary parameters β_x and β_y mainly describe mispointing behaviors. They are rearranged compared to Buchhaupt et al. [14] (Equation (53)) to mitigate numerical instabilities for yaw angles close to 90° or 270° (observed mainly in Sentinel-6MF cycles 23 and 24), causing tangents and secant terms to become infinite. In this study, β_x and β_y are given as

$$\beta_x = \sqrt{\frac{c}{\alpha_x h_s}}\frac{2}{h_s}\left(a^2 \cos \xi_y \Delta x + b^2 \sin \xi_y \Delta y\right) \tag{A7a}$$

$$\beta_y = \sqrt{\frac{c}{\alpha_y h_s}}\frac{2}{h_s}\left(b^2 \cos \xi_y \Delta y - a^2 \sin \xi_y \Delta x\right) \tag{A7b}$$

where Δx and Δy describe the along- and across-track positions of the antenna's maximum gain with respect to the reference torus. They are given by

$$\Delta x = x_s \cos \xi_y - h_s \tan \xi_p - y_s \sin \xi_y \tag{A8a}$$

$$\Delta y = y_s \cos \xi_y - h_s \tan \xi_r - x_s \sin \xi_y \tag{A8b}$$

Appendix B. Probability Density Function

The PDF term derivation is thoroughly described in Buchhaupt et al. [9]. However, for the sake of completeness, we provide a less approximated version here—including the reciprocal absolute value of the denominator terms of exponential arguments—given as

$$\begin{aligned} P\hat{\hat{D}}F(f,t_s) &\approx \frac{\Delta A\ \exp\{-2\pi i\bar{t}_0 f\}}{\sqrt{\left(1+4\pi^2\mu^2\sigma_t^2t_s^2\right)^2+4\pi^2\mu_s^2\sigma_s^2f^2}} \\ &\times \exp\left\{\frac{-2\pi^2\sigma_s^2f^2[1-6\mu_s\mu]}{1-2\pi i\mu_s\sigma_sf+4\pi^2\mu^2\sigma_t^2t_s^2}\right\} \\ &\times \exp\left\{\frac{-2\pi^2\sigma_t^2t_s^2\left[1+2\pi i\mu(1+\nu)\sigma_sf-4\mu^2\right]}{1-2\pi i\mu_s\sigma_sf+4\pi^2\mu^2\sigma_t^2t_s^2}\right\} \end{aligned} \tag{A9}$$

where ΔA is the amplitude factor, σ_t is the attenuated standard deviation of vertical wave-particle velocities converted into Doppler-frequency blurring, and $\bar{t}_0$ is the mean epoch affected by an electromagnetic bias (EMB). They are given as

$$\Delta A = 1+4\mu^2 \tag{A10a}$$

$$\sigma_t = \frac{2}{\lambda_c}a_v\,\sigma_v \tag{A10b}$$

$$\bar{t}_0 = t_0+2\mu\sigma_z = t_0+\frac{2}{g}\sigma_v^2 \tag{A10c}$$

However, in this study, a simplified PDF was used, neglecting the non-linear term affecting the vertical wave-particle velocities, given as

$$\begin{aligned} P\hat{\hat{D}}F(f,t_s) &\approx \frac{1}{\sqrt{1+4\pi^2\mu_s^2\sigma_s^2f^2}} \\ &\times \exp\left\{-2\pi i\bar{t}_0f-2\pi^2\sigma_t^2t_s^2\right\} \\ &\times \exp\left\{\frac{-2\pi^2\sigma_s^2f^2[1-6\mu_s\mu]}{1-2\pi i\mu_s\sigma_sf}\right\} \end{aligned} \tag{A11}$$

It was shown by Buchhaupt et al. [9] that this approximation provides sufficiently accurate σ_v estimates.

Appendix C. Point Target Response

The PTR in the frequency/slow-time domain is defined by the two-dimensional auto-correlation—represented by the $\star\star$ operator—given in Buchhaupt et al. [14] (Equation (57)) as

$$P\hat{\hat{T}}R(f,t_s) = \left[\frac{\sqcap\left(\frac{t_s^*}{\tau_b}\right)}{1+\frac{f}{f_c}}\sqcap\left(\frac{f}{B}\right)\right]\star\star\left[\frac{\sqcap\left(\frac{t_s^*}{\tau_b}\right)}{1+\frac{f}{f_c}}\sqcap\left(\frac{f}{B}\right)\right] \tag{A12}$$

An analytical solution for the PTR can be found, but since it is constant for each satellite altimeter mission, it is feasible to compute it numerically at the start of each processing campaign. In this study, it is computed in the following way:

$$P\hat{T}R(f,f_D) = \mathcal{F}_\tau^{-1}\left\{\left|\mathcal{F}_\tau\left\{\frac{\sin\left(\pi\tau_b\left[1+\frac{f}{f_c}\right]f_D\right)}{\pi\tau_b\left[1+\frac{f}{f_c}\right]f_D}\sqcap\left(\frac{f}{B}\right)\right\}\right|^2\right\} \tag{A13}$$

where $\mathcal{F}_\tau$ describes a forward Fourier transform from the frequency to the time-delay domain and $\mathcal{F}_\tau^{-1}$ describes its inversion.

The slow-time shift $t_s \mapsto t_s+\frac{f}{s}$ is then applied by

$$P\hat{\hat{T}}R\left(f,t_s+\frac{f}{s}\right) = \mathcal{F}_x^{-1}\left\{P\hat{T}R(f,f_D)\,\exp\left\{2\pi i\frac{f}{s}f_D\right\}\right\} \tag{A14}$$

where $\mathcal{F}_x^{-1}$ describes a backward Fourier transform from the Doppler frequency to the slow-time domain.

References

1. Brown, G. The average impulse response of a rough surface and its applications. *IEEE Trans. Antennas Propag.* **1977**, *25*, 67–74. [CrossRef]
2. Amarouche, L.; Thibaut, P.; Zanife, O.Z.; Dumont, J.P.; Vincent, P.; Steunou, N. Improving the Jason-1 Ground Retracking to Better Account for Attitude Effects. *Mar. Geod.* **2004**, *27*, 171–197. [CrossRef]
3. Chelton, D.B.; Walsh, E.J.; MacArthur, J.L. Pulse compression and sea level tracking in satellite altimetry. *J. Atmos. Ocean. Technol.* **1989**, *6*, 407–438. .<0407:PCASLT>2.0.CO;2. [CrossRef]
4. Egido, A.; Smith, W.H.F. Fully Focused SAR Altimetry: Theory and Applications. *IEEE Transactions on Geoscience and Remote Sensing* **2017**, *55*, 392–406. [CrossRef]
5. Kleinherenbrink, M.; Naeije, M.; Slobbe, C.; Egido, A.; Smith, W. The performance of CryoSat-2 fully-focussed SAR for inland water-level estimation. *Remote Sens. Environ.* **2020**, *237*, 111589. [CrossRef]
6. Raney, R. SAR response to partially coherent phenomena. *IEEE Trans. Antennas Propag.* **1980**, *28*, 777–787. [CrossRef]
7. Ray, C.; Martin-Puig, C.; Clarizia, M.P.; Ruffini, G.; Dinardo, S.; Gommenginger, C.; Benveniste, J. SAR Altimeter Backscattered Waveform Model. *IEEE Trans. Geosci. Remote Sens.* **2015**, *53*, 911–919. [CrossRef]
8. Buchhaupt, C. Model Improvement for SAR Altimetry. Ph.D. Thesis, Technische Universität, Darmstadt, Germany, 2019.
9. Buchhaupt, C.; Egido, A.; Smith, W.H.; Fenoglio, L. Conditional sea surface statistics and their impact on geophysical sea surface parameters retrieved from SAR altimetry signals. *Adv. Space Res.* **2023**, *71*, 2332–2347. [CrossRef]
10. Raynal, M.; Cadier, E.; Labroue, S.; Moreau, T.; Féménias, P.; Boy, F.; Picot, N.; Scharroo, R.; Borde, F. Lessons learned from Sentinel SARM missions in preparation of Jason-CS. In Proceedings of the Ocean Surface Topography Science Team Meeting (OSTST) 2019, Chicago, IL, USA, 21-25 October 2019.
11. Egido, A.; Buchhaupt, C.; Boy, F.; Maraldi, C.; Cadier, E.; Dinardo, S.; Leuliette, E.; Moreau, T. A Significant Wave Height Correction to Account for Vertical Wave Motion Effects in SAR Altimeter Measurements. In Proceedings of the 2022 Ocean Surface Topography Science Team Meeting, Lido, Italy, 31 October–4 November 2022. [CrossRef]
12. Mouche, A.A.; Chapron, B.; Reul, N.; Collard, F. Predicted Doppler shifts induced by ocean surface wave displacements using asymptotic electromagnetic wave scattering theories. *Waves Random Complex Media* **2008**, *18*, 185–196. [CrossRef]
13. Buchhaupt, C.; Fenoglio-Marc, L.; Dinardo, S.; Scharroo, R.; Becker, M. A fast convolution based waveform model for conventional and unfocused SAR altimetry. *Adv. Space Res.* **2018**, *62*, 1445–1463. [CrossRef]
14. Buchhaupt, C.; Fenoglio, L.; Becker, M.; Kusche, J. Impact of vertical water particle motions on focused SAR altimetry. *Adv. Space Res.* **2020**, *68*, 853–874. [CrossRef]
15. Chapron, B.; Collard, F.; Kerbaol, V. Satellite Synthetic Aperture Radar Sea Surface Doppler Measurements. In *Proceedings of the 2nd Workshop on SAR Coastal and Marine Applications*; Lacoste, H., Ed.; ESA Special Publication: Noordwijk, The Netherlands, 2004; Volume 565, p. 14.
16. Kunis, S. *Nonequispaced FFT: Generalisation and Inversion*; Berichte aus der Mathematik: Shaker, Düren/Maastricht, Germany, 2007.
17. Bluestein, L. A linear filtering approach to the computation of discrete Fourier transform. *IEEE Trans. Audio Electroacoust.* **1970**, *18*, 451–455. [CrossRef]
18. Holland, A.C. The effects of atmospheric refraction on angles measured from a satellite. *J. Geophys. Res.* **1961**, *66*, 4171–4175.
19. Rüger, J. Refractive Index Formulae for Radio Waves. In Proceedings of the FIG XXII International Congress, Washington, DC, USA, 19–26 April 2002.
20. Murray, F.W. On the Computation of Saturation Vapor Pressure. *J. Appl. Meteorol. Climatol.* **1967**, *6*, 203–204. .<0203:OTCOSV>2.0.CO;2. [CrossRef]
21. Scagliola, M.; Recchia, L.; Maestri, L.; Giudici, D. Evaluating the impact of range walk compensation in delay/Doppler processing over open ocean. *Adv. Space Res.* **2021**, *68*, 937–946. [CrossRef]
22. Marquardt, D.W. An algorithm for least-squares estimation of nonlinear parameters. *SIAM J. Appl. Math.* **1963**, *11*, 431–441. [CrossRef]
23. Pierson Jr., W.J.; Moskowitz, L. A proposed spectral form for fully developed wind seas based on the similarity theory of S. A. Kitaigorodskii. *J. Geophys. Res.* **1964**, *69*, 5181–5190. [CrossRef]
24. Copernicus Climate Change Service, Climate Data Store. ERA5 Hourly Data on Single Levels from 1940 to Present. Copernicus Climate Change Service (C3S) Climate Data Store (CDS). 2023. https://doi.org/10.24381/cds.adbb2d47 (accessed on 27 March 2023).
25. Leys, C.; Ley, C.; Klein, O.; Bernard, P.; Licata, L. Detecting outliers: Do not use standard deviation around the mean, use absolute deviation around the median. *J. Exp. Soc. Psychol.* **2013**, *49*, 764–766. [CrossRef]
26. Edson, J.B.; Jampana, V.; Weller, R.A.; Bigorre, S.P.; Plueddemann, A.J.; Fairall, C.W.; Miller, S.D.; Mahrt, L.; Vickers, D.; Hersbach, H. On the Exchange of Momentum over the Open Ocean. *J. Phys. Oceanogr.* **2013**, *43*, 1589–1610. [CrossRef]

27. Takagaki, N.; Komori, S.; Suzuki, N. Estimation of friction velocity from the wind-wave spectrum at extremely high wind speeds. *IOP Conf. Ser. Earth Environ. Sci.* **2016**, *35*, 012009. [CrossRef]
28. Brown, G.S. *Reduced Backscattering cross Section (σ^0) Data from the Skylab S-193 Radar Altimeter*; Technical Report, NASA-CR-141401; Wallops Flight Center: Wallops Island, VA, USA, 1975.